Aqueous surface layer flows induced by microscale breaking wind waves

By WILLIAM L. PEIRSON† AND MICHAEL L. BANNER

School of Mathematics, The University of New South Wales, Sydney, Australia

Microscale breaking wind waves cover much of the surface of open waters exposed to moderate wind forcing. Recent studies indicate that understanding the nature and key features of the surface skin flows associated with these small waves is fundamental to explaining the dramatic enhancement of constituent exchange that occurs in their presence. We describe a laboratory study in which velocity measurements were made within a few hundred micrometres of the surface of microscale breaking wind waves without bubble entrainment, using flow visualization and particle image velocimetry (PIV) techniques for a range of wind speed and fetch conditions. Our measurements show that for each experiment, the mean surface drift directly induced by the wind on the upwind faces and crests of these waves is $(0.23 \pm 0.02)u_*^a$ in the trough increasing to $(0.33 \pm 0.07)u_*^a$ at the crest, where u_*^a is the wind friction velocity. About these mean values, there is substantial variability in the instantaneous surface velocity up to approximately $\pm 0.17u_*^a$ in the trough and $\pm 0.37u_*^a$ at the crest. This variability can be attributed primarily to the modulation of the wave field, with additional contributions arising from fluctuations in wind forcing and near-surface turbulence generated by shear in the drift layer or by the influence of transient microscale breaking.

We observed that in a frame of reference travelling with a microscale breaking wave, the transport in the aqueous surface layer is rearward along its entire surface, except within and immediately upwind of the spilling region. Moreover, we found that transport of surface fluid rarely occurs forward over the crest and into the spilling region. This is in marked contrast with previously envisaged wind drift layer flow structures. Visualizations and PIV measurements demonstrate the important role of microscale wind-wave breaking in the direct transport of fluid from the surface to the highly turbulent domain below. Many hundreds of surface flow visualization images were carefully examined. These showed that at the toe of each microscale breaker spilling region, there is an intense and highly localized convergence of surface fluid, with convergence rates generally exceeding $100\,\mathrm{s}^{-1}$. By comparison, observations of surface convergence attributable to parasitic capillary activity are modest. The changes in mean surface drift along the upwind faces of the waves are equivalent to mean surface divergences of between 0.2 and $1.3\,\mathrm{s}^{-1}$. Flow visualizations of the surface layer along the upwind (windward) faces of these waves revealed the occurrence of locally intense flow divergence. However, maximum values of the divergence rate were observed to be only of order $10\,\mathrm{s}^{-1}$. Hence these divergence zones are much more diffuse than the convergence zones at the toes of spilling regions.

  † Present address: Water Research Laboratory, School of Civil and Environmental Engineering, The University of New South Wales, Sydney, Australia; W.Peirson@unsw.edu.au

Overall, our measurements strongly support the view that microscale breaking is likely to be the dominant process in the enhancement of sea surface exchange at moderate wind speeds, as has been suggested by a number of previous investigators. Using a simple model based on our observations, it is shown that microscale breaking is potentially a very effective process in the observed enhancement of constituent transfer for $U_{10} \geqslant 4\,\mathrm{m\,s^{-1}}$ (where U_{10} is wind speed measured 10 m above the surface) and this mechanism exceeds by a wide margin the strength of other previously proposed mechanisms.

1. Introduction

Once the wind speed exceeds approximately $3.8\,\mathrm{m\,s^{-1}}$ measured at 10 m above natural water surfaces that are free of surface slicks, microscale breaking waves develop and cover much of the surface (Katsaros & Ataktürk 1992). At very short fetches, these microscale breaking wind waves can dominate the wave spectrum and, even in open ocean wind seas, the water surface remains covered by them (e.g. Banner, Jones & Trinder 1989). These microscale breakers have typical wavelengths of between 50 and 300 mm but are less conspicuous than their more visible, larger-scale counterparts known as whitecaps, because they have much smaller wavelengths and mostly do not entrain bubbles nor generate spray. Nevertheless, recent investigations have highlighted their potential role in air–sea exchange at moderate wind speeds. Clearer insight into their kinematical behaviour and associated near-surface water motions is essential for understanding and reliable parameterization of interfacial fluxes of constituents.

We report laboratory observations of transport and velocity structure within the viscous aqueous sublayer beneath the surface of microscale breaking wind waves without bubble entrainment. These measurements were made using particle image velocimetry (PIV) techniques based on flow visualizations obtained from specially designed instrumentation (Peirson 1997) with a spatial resolution less than $35\,\mu\mathrm{m}$. A subset of the data presented here was utilized previously to derive the tangential forcing of the surface (Banner & Peirson 1998, hereafter referred to as BP98). Our present observations reveal the intricate and complex processes that occur immediately beneath open water surfaces covered with microscale breaking waves. In particular, the highly localized intense surface convergence and divergence motions observed and reported here are envisaged to play a significant role in the interfacial exchange of constituents.

In their recent review article, Jähne & Haußecker (1998) summarized current understanding of air–water gas exchange as follows:

1. Interfacial exchange is controlled by the aqueous diffusion sublayer, a viscous layer of 20–$200\,\mu\mathrm{m}$ nominal thickness immediately below the surface.

2. Transfer rates are significantly increased in the presence of waves even though air entrainment or droplet generation does not occur. For this regime, systematic increases in transfer rates can be observed with respect to the wind friction velocity and the mean-square slope of the interface but the physical mechanisms responsible for this enhancement have not been identified.

3. Conventional modelling of surface exchange has relied on proposed descriptions of the interaction of turbulence with the surface, within the framework known as surface renewal modelling. However, the relationship between surface waves and near-surface turbulence remains poorly understood.

4. Recent research in this area has utilized novel infrared imaging techniques and spatially extensive particle imaging methods to observe surface heat flux and concomitant near-surface motions and concentrations.

Since Jähne & Haußecker (1998) appeared, detailed observations of surface heat flux, constituent flux and near-surface motions have been reported by a number of investigators, including Jessup, Zappa & Yeh (1997), Zappa, Jessup & Asher (2001) and Siddiqui *et al.* (2001, hereafter referred to as S2001). Jessup *et al.* (1997) gathered infrared images of laboratory air–water interfaces and the open ocean surface, from which they concluded that microscale breaking was responsible for the observed thermal signatures. Zappa *et al.* (2001) reported laboratory measurements using high-resolution infrared imaging over a wind speed range of 4.5 to $11\,\mathrm{m\,s}^{-1}$. Their data set linked the interfacial exchange rate of He and SF_6 to the fractional area coverage of microscale wave breaking events. (The fractional area coverage is defined as the spatial area of a surface infrared image that has a temperature greater than a threshold specified as a function of the temperature standard deviation and coldest temperatures observed in the image). S2001 extended the Zappa *et al.* (2001) study by measuring the accompanying subsurface turbulence field and observed a systematic relationship between exchange rate and fractional area coverage of microscale wave breaking with root-mean-square vorticity in the top 10 mm of the water determined using PIV techniques.

Despite these impressive advances, the underlying physical processes responsible for the strong correlation between the enhanced exchange associated with microscale breaking waves and the fractional area coverage remain to be identified and quantified. With this goal, the present study has focused on the surface skin transport and kinematical aspects of microscale breaking wind waves under laboratory conditions. It quantifies the interaction between wind-induced drift currents at the surface and the microscale breaking waves, as well as the typical intensities of the associated surface flow convergence and divergence processes, thereby identifying the key processes responsible for enhanced exchange. Analyses based on our laboratory observations suggest that subduction at the toe of the spilling region of microscale breakers is the key surface process associated with destruction of the surface sublayers and the generation of vorticity and turbulence at the free surface of open waters under moderate-to-strong wind forcing.

2. Observations of aqueous surface and near-surface processes in the presence of microscale breaking waves

Direct field observations of microscale breaking waves are very difficult to make and investigations have generally been restricted to theoretical studies or suitably designed laboratory experiments. Even so, while laboratory generation of these waves is straightforward due to their rapid development with fetch, there have been relatively few detailed studies of their kinematical behaviour.

Figure 1 shows a representative measured microscale breaking wave profile obtained during this investigation at a fetch of 4.35 m and wind speed of $8.1\,\mathrm{m\,s}^{-1}$. Using the measured wave speed, the recorded waveform has been transformed so that it appears at an approximately undistorted spatial scale. Those aspects of microscale breaking wave kinematics that have been studied previously by other investigators are indicated in figure 1 and are described below.
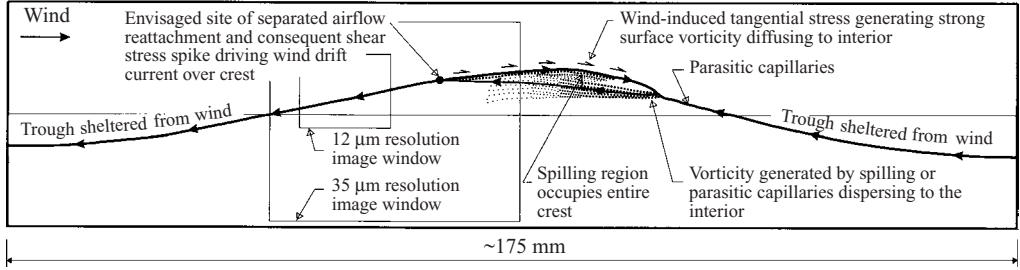
FIGURE 1. Conceptual diagram illustrating previous understanding of the kinematic behaviour of microscale breaking wind waves. In a frame of reference moving with the wave, transport is rearward except within the wave crest. Strong surface tangential stresses from the point of airflow reattachment induce transport up the windward face and over the crest. Subsurface vorticity is generated by the tangential stresses as well as by parasitic capillary structures and spilling breaking. In this diagram the significant features are annotated and the PIV window sizes used for this investigation are shown.

(i) *Transport of surface particles*

A number of investigators have reported that the mean surface transport both in the presence and absence of microscale breaking wind waves is given by $(0.55 \pm 0.1)u_*^a$ (e.g. Keulegan 1951; Phillips & Banner 1974; Wu 1975; amongst others). However, what remains unresolved is the relative contribution to the total drift of each of the various fundamental transport processes (wind-induced drift, windage (motion induced by wind drag on surface emergent surfaces), Lagrangian drift and entrainment within the spilling regions).

(ii) *Distributions of surface velocity and wind-induced tangential stress*

Okuda, Kawai & Toba (1977, henceforth referred to as O77) and Okuda (1982, henceforth referred to as O82) published the first systematic studies of wind-induced drift in the presence of microscale breaking waves, reporting measurements of surface tangential stress and surface velocity distributions. On the basis of hydrogen bubble measurements, O77 concluded that very intense tangential stresses were induced by the wind at the wave crests. O82 subsequently investigated the subsurface vorticity field and obtained estimates of surface velocity derived from cine camera images of the motion of hydrogen bubbles and small floating beads. O82 also used hydrogen bubbles to measure surface velocity distributions along the surfaces of a set of three individual waves (figure 2) and on that basis concluded that the crest surface velocity was in excess of the wave celerity for a substantial proportion of waves (figure 1). However, as shown in figure 2, measurements in the critical phase region between $-45°$ and $+10°$ were not possible and the results of O77 were used to infer that the fluid velocity at the crest is greater than the wave speed.

O82 only made measurements of three individual waves, yet there is a distribution of wave heights due to wave group structure and hence it is important to consider whether these waves are representative of the overall wave population. O82 tabulated the heights of these three individual waves relative to the significant wave height (the mean of the largest 1/3 of all waves) and observed that cases II and III were breaking. Using the O82 values and comparing them with wave populations from our measurements (described in §3.2 below), the proportion of waves exceeding the height of case II and III waves were 1% and 6% respectively. On the basis of wave
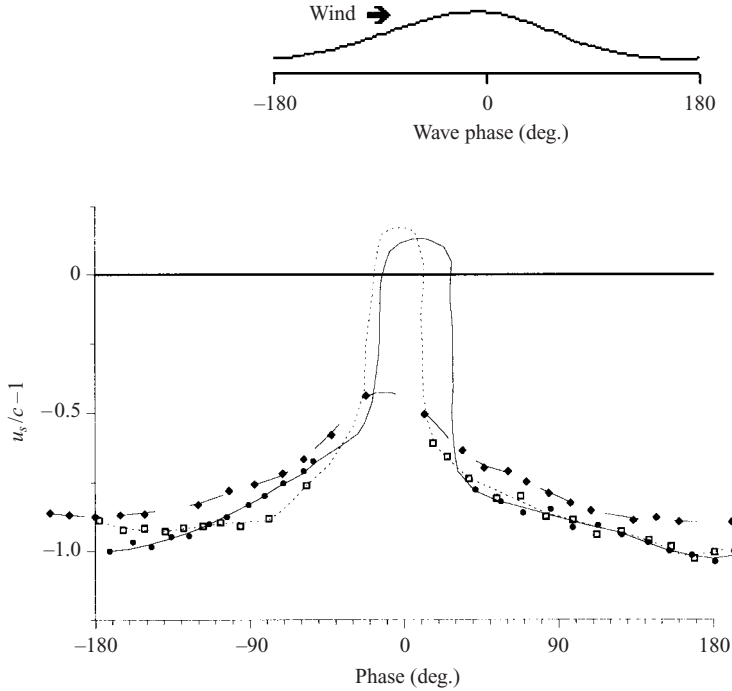
FIGURE 2. Surface velocity distributions along the wave inferred from hydrogen bubble measurements by Okuda (1982) at a fetch of 6 m and a wind speed of $5.0\,\mathrm{m\,s^{-1}}$. The measured data points are indicated by the symbols, with lines indicating the interpolations. Measurement cases and approximate relative wave heights: ●, —, case II ($H_{1\%}$); □, ..., case III ($H_{6\%}$); ◆, −−−, case IV($H_{60\%}$), ($H_{x\%}$ is the height of a wave in a population in which $x\%$ are larger.) Note the absence of measured data between phases of $-45°$ to $+10°$ for the larger waves.

statistics alone, case II and III waves represent examples of extremely steep waves within the overall wave population.

Recently, BP98 questioned the magnitude of the very strong tangential stresses reported by O77 at the crests of wind-forced microscale breaking waves. BP98 argued that the intensity of tangential stresses reported by O77 may have been an artefact of the hydrogen bubble technique they used to determine the shear in the aqueous viscous sublayers. Similar concerns apply to the conclusions of O82 regarding surface transport in the vicinity of the crests of microscale breaking wind waves.

(iii) *Breaking*

In his recent review of spilling breaking, Duncan (2001, p. 543) states that the effect of wind drift on short-wavelength breakers is an area requiring further research. Banner & Phillips (1974) proposed a theoretical model of the initiation of breaking induced by the wind drift current at wave crests, but to our knowledge, no other investigations have been published on the detailed kinematics associated with microscale wave breaking in the presence of wind. Previous studies have been limited to the kinematics of the spilling region in the absence of wind. Such studies include, the following.

(*a*) An analysis of the dynamics of the spilling region and the momentum flux associated with wave breaking based on a similarity model (Longuet-Higgins & Turner 1974).

(*b*) Identifying spilling breakers as composed of two regions of distinct flow (the spilling region and the underlying flow), linked by a thin layer of very high shear similar to the upstream condition of a conventional turbulent mixing layer (Peregrine & Svendsen 1978). By flow visualization, they showed that the thickness of this shear layer rapidly increases due to intense turbulence production (see figure 1).

(*c*) Use of a towed hydrofoil to generate breaking waves with air entrainment (Duncan 1981). For a range of hydrofoil speeds and angles of attack, the behaviour of the waves and injected dye streaks was captured by optical methods and a turbulent shear layer was observed that persisted well into the wake of the breaking wave.

(*d*) Measurements within the spilling regions of stationary breaking waves in a flowing current in the absence of wind (Banner 1988). A surface gravity wave train was formed by a surface deflection plate located well upstream, with the breaking strength controlled by adjusting the angle of incidence to the flow of a subsurface hydrofoil. Measurements using a single-component laser Doppler anemometer revealed that (i) the spilling region did not extend to the crest of the wave as had been assumed previously, (ii) intense levels of mean subsurface shear ($\sim 180\,\mathrm{s}^{-1}$) existed at the toe of the spilling region, (iii) high levels of fluctuating velocity ($\sim 25\%$ of the wave speed) occurred within the spilling region, (iv) momentum is diffused rapidly into the subsurface flow rearward from the toe, driving a surface shear layer.

(*e*) PIV measurements in stationary waves induced by steady flow past a subsurface hydrofoil inclined at $30°$ to the incident flow (Lin & Rockwell 1995). Conditions ranged from non-breaking to incipient breaking with the development of parasitic capillaries on the forward face and extended to intense breaking with a large separation region beneath the forward face of the wave. For strongly breaking wave conditions, they measured levels of shear immediately behind the toe of the spilling region as high as $456\,\mathrm{s}^{-1}$.

(iv) *Parasitic capillary wave behaviour*

Steep, small-scale gravity waves are usually accompanied by parasitic capillary waves on their forward faces (figure 1). Through detailed theoretical studies, Longuet-Higgins and his co-workers have made significant contributions to our understanding of the dynamics of these waves in the absence of wind. The most theoretical descriptions of parasitic capillary waves and their interaction with gravity waveforms are given in Longuet-Higgins (1992, 1995). These papers show that the interaction of surface tension with local acceleration of the surface fluid on the forward face of the waves is conducive to parasitic capillary wave formation.

Longuet-Higgins (1992) postulated that interaction between parasitic capillary waves and the gravity wave crest would lead to the formation of secondary capillary waves and the initiation of surface breaking. This has been verified experimentally by Duncan *et al*. (1994). The study of Lin & Rockwell (1995) also included one case of a very steep wave with parasitic capillaries present. Their study verified the presence of regions of alternating vorticity beneath the crests and troughs of these waves, as predicted by Longuet-Higgins (1992).

More recent work by Federov & Melville (1998) has developed a new theoretical approach to nonlinear gravity–capillary wave behaviour, which was demonstrated to be in good agreement with experimental observations by Federov, Melville & Rozenberg (1998).

3. Measurement conditions

The measurements reported here were undertaken to determine the surface velocity structure of breaking microscale wind waves for a range of wind speed and fetch conditions. This entailed probing aqueous viscous sublayers substantially less than a millimetre deep below a water surface covered in waves with heights of a centimetre or more. In the present investigation, our focus was on propagating wind-generated waves and therefore observations were complicated by the unsteady motion of the waves past the observation point. As discussed in Melville (1994) and Peirson & Banner (2000), there appear to be some important dynamical differences in the breaking strengths of stationary and propagating breaking waves and we wished to avoid such issues.

The measurement system is documented in detail in Peirson (1997) and the experimental conditions in BP98. In brief, our study was conducted in a wind-wave tank 220 mm wide and 8 m long, with a wind tunnel section transitioning smoothly over the water surface. The water depth was 200 mm with a 420 mm high air channel above. Measurements were made at two fetches and three wind speeds. The wind wavelets generated at these very short fetches were generally in a state of microscale breaking and their propagation properties vary strongly with fetch and wind speed. However, at the shortest fetch (2.35 m) and lowest wind speed (4.8 m s^{-1}), no microscale breaking wind waves were present. The maximum fetch attainable was 4.35 m: the shorter fetch was achieved by shielding the water surface with a thin ($< 200\,\mu$m thickness) floating membrane. All relevant details of the wind and wave properties are summarized in table 1 and all row references in this paper refer to this table.

3.1. *Air flow*

Referring to table 1, the local wind forcing of the surface due to a centreline wind speed U_{cl} (row 2) was quantified in terms of the wind friction velocity u_*^a (row 3) and the aerodynamic roughness length z_0^a (row 4). These quantities were determined for each experiment using the standard method of characterizing the logarithmic region of the mean velocity profile measured in the airflow. The total wind stress (ρu_*^{a2}) is shown in row 5. For completeness, the mean tangential stress as determined by BP98 is included in row 6.

3.2. *Waves*

Measuring the propagation characteristics of these microscale waves is complicated by their advection by the wind drift current, but we developed a technique that provided a direct measure of individual wave speeds. A summary of the measured wave properties is given in table 1 and details of the measurement methodology are described in the Appendix.

The measured total speeds of individual characteristic waves were averaged to obtain a mean total speed for the entire population c_{eff} (row 14). As shown in the Appendix, the product of an individual total wave speed and the corresponding observed wave period gives a local wavelength. The mean wavelength for each experiment is shown in row 17. The mean wavelength was also measured from ensembles of photographs of representative wave profiles. These two independent wavelength estimates were in agreement to within $\pm 20\%$. Measurement of local wave heights yielded a mean height (row 16) as well as mean and root-mean-square (r.m.s) wave steepnesses (rows 18 and 19).

		Error($\pm$)					
1	Fetch (m)	<1%	4.35	2.45	4.35	2.45	4.35
	Wind forcing						
2	U_{cl} (m s^{-1})	2%	4.8	6.3	6.3	8.1	8.1
3	u_*^a (m s^{-1})	10%	0.26	0.32	0.37	0.40	0.46
4	z_o^a (mm)	50%	0.160	0.031	0.177	0.081	0.151
5	τ(Pa)	20%	0.083	0.125	0.168	0.199	0.261
6	τ_{tang}(Pa)	15%	0.049	0.069	0.074	0.082	0.077
	Wave characteristics						
	All waves						
7	Energy (mm^2)	4%	4.85	6.77	14.90	16.14	30.82
8	Mean frequency (Hz)	2%	5.06	5.37	3.86	4.17	3.33
9	Mean height [mm]	2%	5.42	6.24	10.10	10.13	14.27
	Ripples						
10	Number		226	289	157	208	198
11	Mean frequency (Hz)	5%	8.19	7.88	5.23	5.90	4.43
12	Mean height (mm)	4%	2.56	3.38	5.25	5.51	8.08
	Distinguishable Waves						
13	Number		1594	1643	1232	1293	998
14	c_{eff} (m s^{-1})	2%	0.361	0.385	0.468	0.476	0.545
15	Mean frequency (Hz)	2%	4.80	5.09	3.74	3.99	3.17
16	Mean height (mm)	2%	6.04	6.97	10.77	11.00	15.69
17	Mean wavelength (m)	2%	0.078	0.078	0.127	0.121	0.174
18	Mean ak	1%	0.245	0.281	0.266	0.285	0.283
19	r.m.s. ak	1%	0.264	0.294	0.276	0.291	0.293
20	Percentage breaking	4%	53	87	70	95	89
21	Std. dev. of akc	4%	0.043	0.050	0.052	0.053	0.071
	Surface velocities						
22	No. of observations		137	142	135	146	135
	Near-surface velocities						
23	No. of images processed		31	49	42	42	46

TABLE 1. Summary of the experimental conditions and mean results.

Using the local wavelength and steepness, equivalent linear and finite wave steepness phase speeds (Longuet-Higgins 1978) can be calculated. However, resolution of the relative contributions of wave propagation speed and drift current was not necessary for this investigation. The issue of primary importance in our study was to identify regions along the wave surface where the surface skin fluid is moving faster than the waveform itself. Relative to a stationary observer, the mean total speed of the waveform is the intrinsic wave speed plus advection by an underlying drift current and is denoted here as c_{eff}.

These detailed measurements of individual waves allow measured waveforms to be averaged in terms of wave phase. These have been normalized by half the wave height and are shown in figures 3(a) to 7(a). In these figures, the averaged waveforms are presented in comparison to the surface profiles of comparable fifth-order Stokes waves. The fifth-order corrections to surface elevation remained less than 1% at the crests and troughs for the measured wave steepness. The actual wave profiles have been offset slightly so that the zero-crossing points coincide approximately.

It can be observed that the averages of the actual wave profiles have slightly narrower crests and broader troughs than their theoretical Stokes wave counterparts. Also, there is a notable asymmetry associated with the measured waves that decreases with fetch and does not appear to be strongly dependent on wind speed in this coordinate system. At the longer fetch, the windward faces of these waves conform
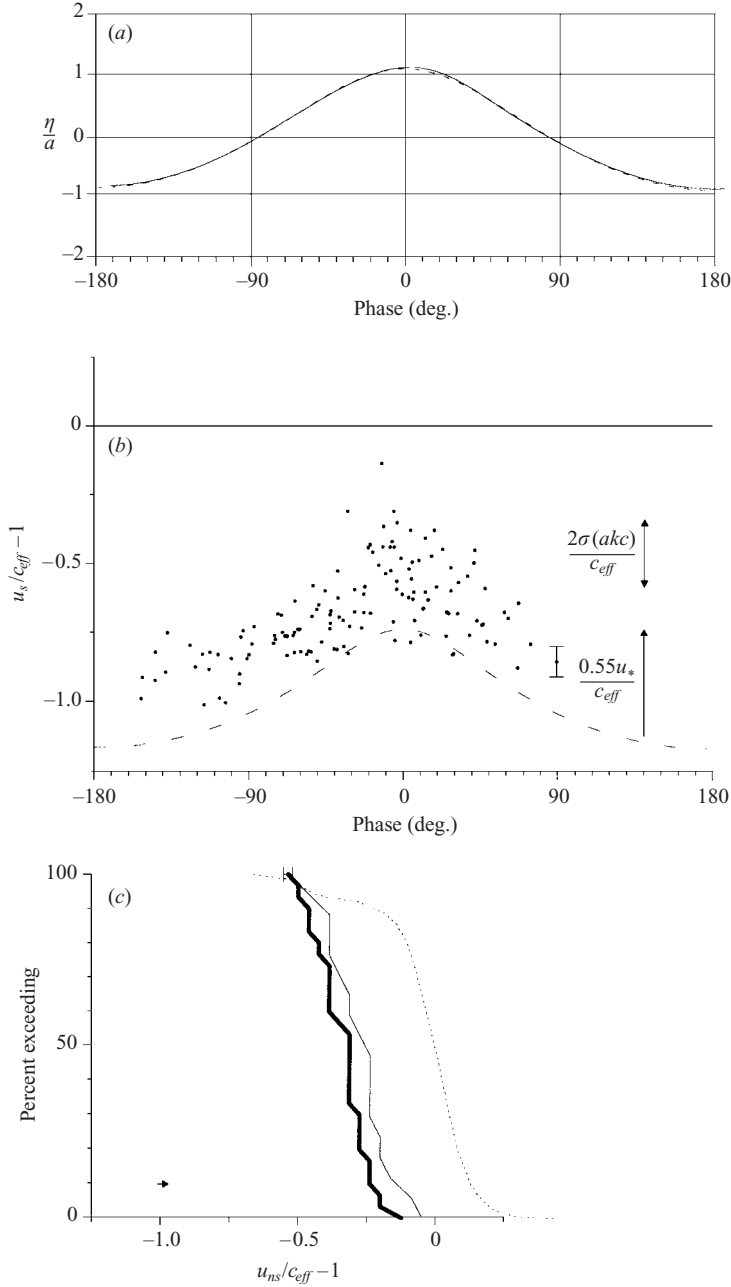
FIGURE 3. Measurements obtained at a fetch of 4.35 m and wind speed of $4.8\,\mathrm{m\,s^{-1}}$. (a) Average waveform (solid line) compared with a fifth-order Stokes waveform for a wave of comparable mean steepness (dashed line). (b) Normalized surface velocity measurements from BP98 (●) as a function of the wave phase with error bars indicated on rightmost point. The surface velocity distribution for a fifth-order Stokes wave is shown as a dashed line. Vertical bars indicate the variability in crest velocity expected by applying linear theory to the measured waveform and the magnitude of the total surface drift obtained from measurements of small floating particles reported by other researchers. (c) Normalized velocity distributions: dotted line – total wave speed; thick solid line – near-surface crest velocities; thin solid line – near-surface velocities downwind of the crest. The normalizing velocity c_{eff} is the measured mean speed of the waves.
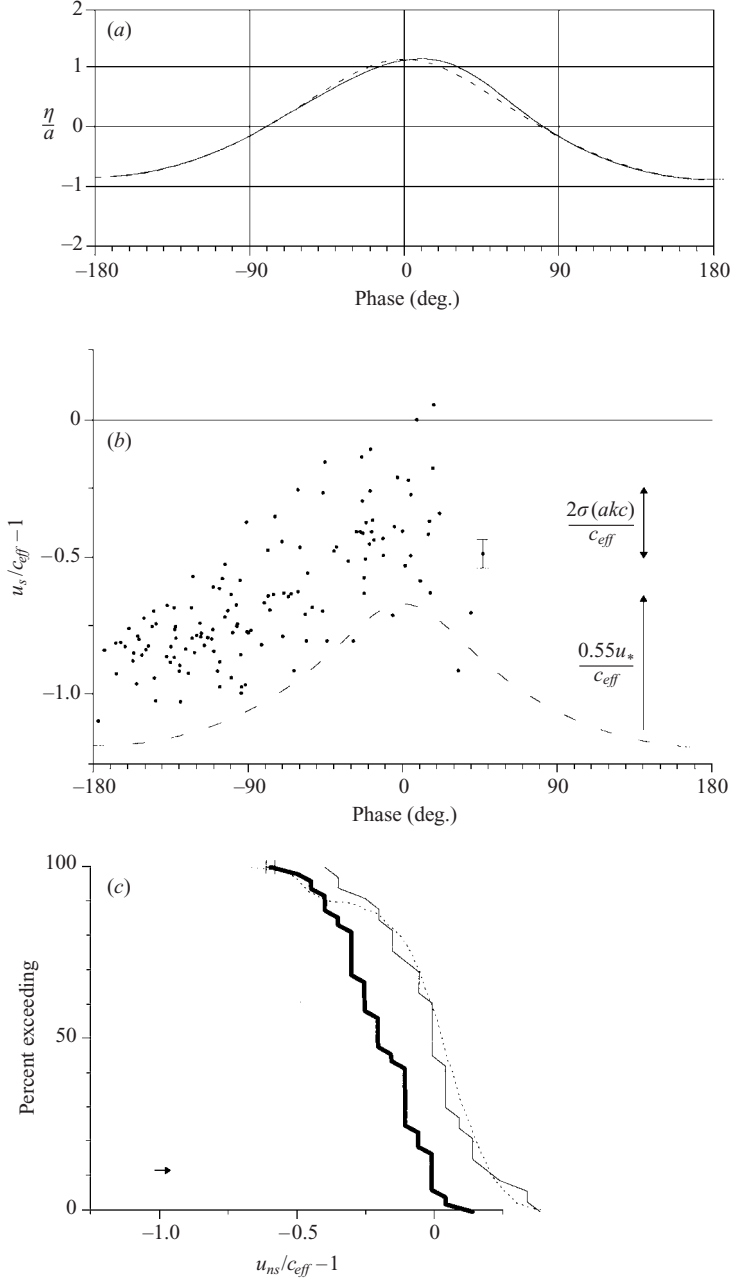
FIGURE 4. As figure 3 but at a fetch of 2.45 m and a wind speed of $6.3\,\mathrm{m\,s}^{-1}$.

reasonably well to the Stokes form. In all cases, the leeward faces show substantially higher slopes than the windward faces, with the differences being more pronounced at shorter fetch.

4. Velocity and flow field measurements

This section describes in detail the surface and near-surface flow fields obtained from a specially designed PIV measurement system. Surface velocities were measured using
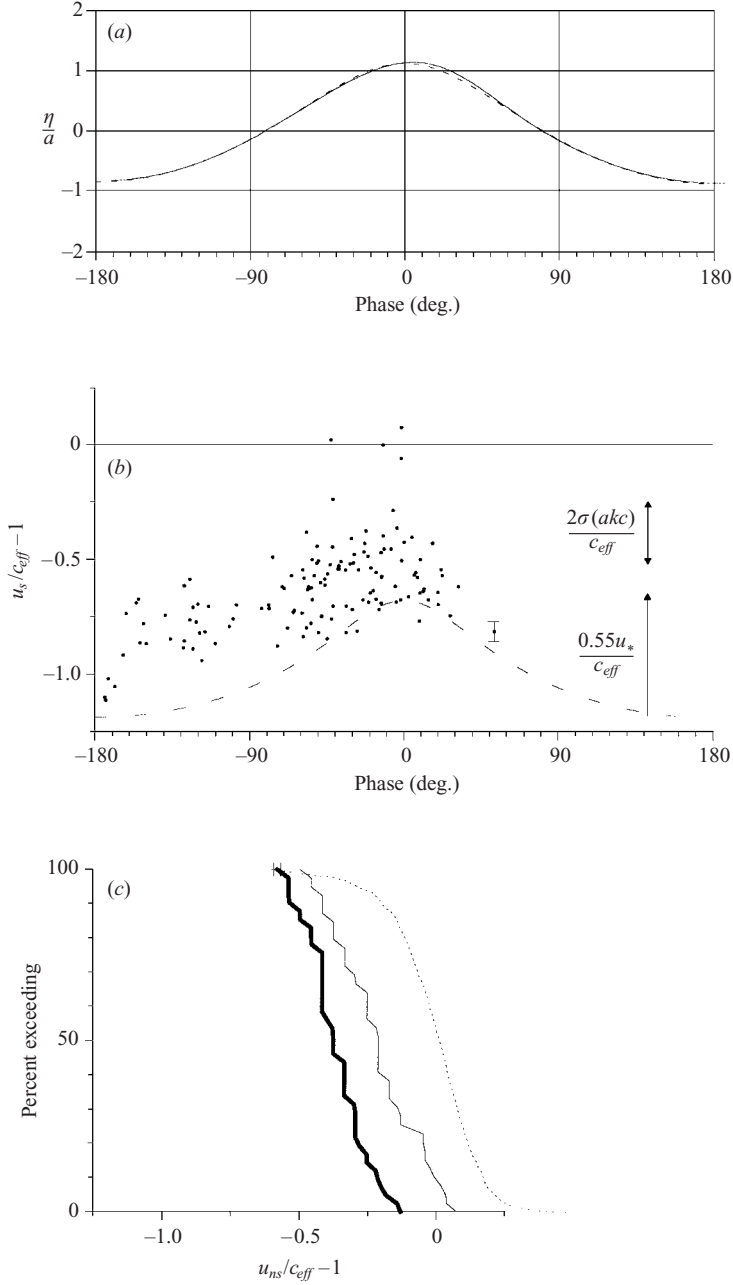
FIGURE 5. As figure 3 but at a fetch of 4.35 m and a wind speed of $6.3\,\mathrm{m\,s^{-1}}$.

the specialized particle image velocimetry (PIV) system developed by Peirson (1997) to measure water velocities within a few hundred micrometres of the local interface. A Kodak *Megaplus* CCD camera with an effective resolution of 1280 (horizontal) by 1024 (vertical) pixels was fitted with a low-distortion lens. This system captured the motion of fluorescent particles (diameters 20–60 μm, mean relative density 1.2) illuminated by pulsing a laser sheet at approximately 500 Hz.
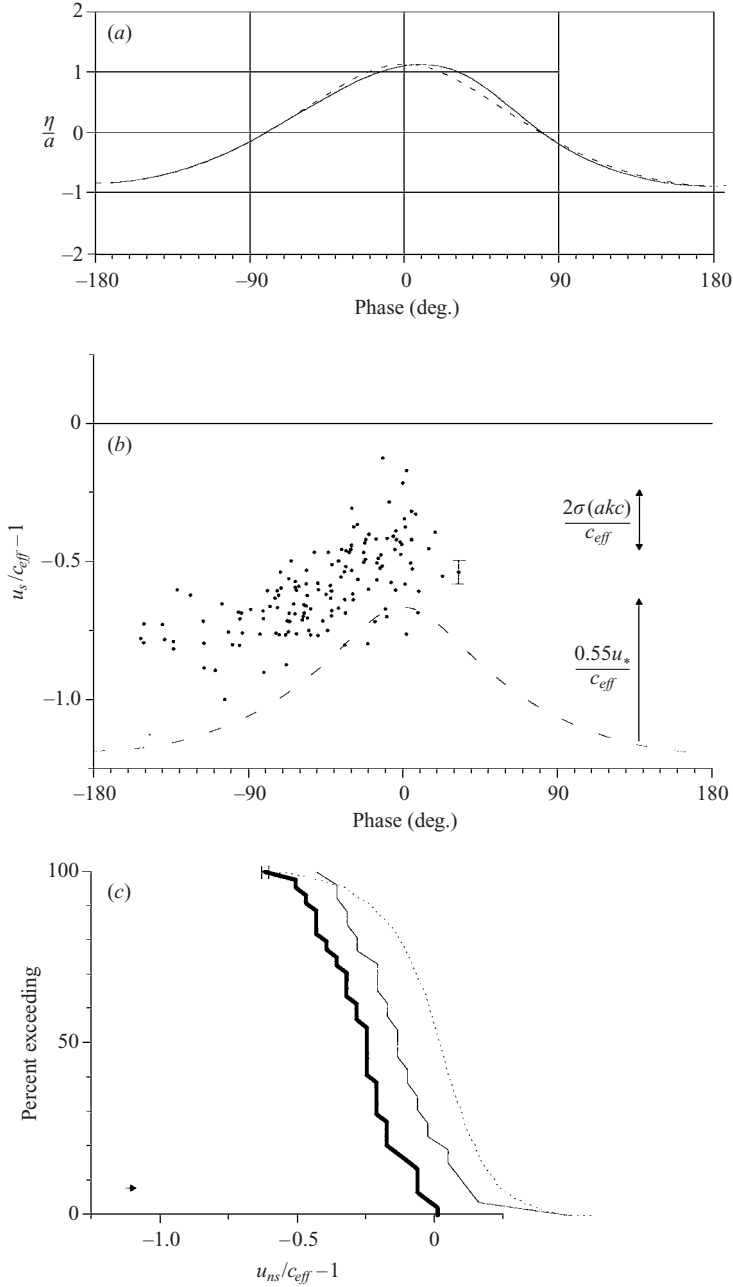
FIGURE 6. As figure 3 but at a fetch of 2.45 m and a wind speed of $8.1 \, \mathrm{m \, s^{-1}}$.

Coincident flow visualization and wave recordings were not possible. The high resolution and consequent size of the captured images meant that a very considerable time interval (approximately 10 s) was required to store each of the visualization images. This precluded any meaningful synchronization with the wave probe data.

The aqueous viscous sublayers have vertical dimensions substantially less than 1 mm but their characteristics are determined by localized processes distributed along
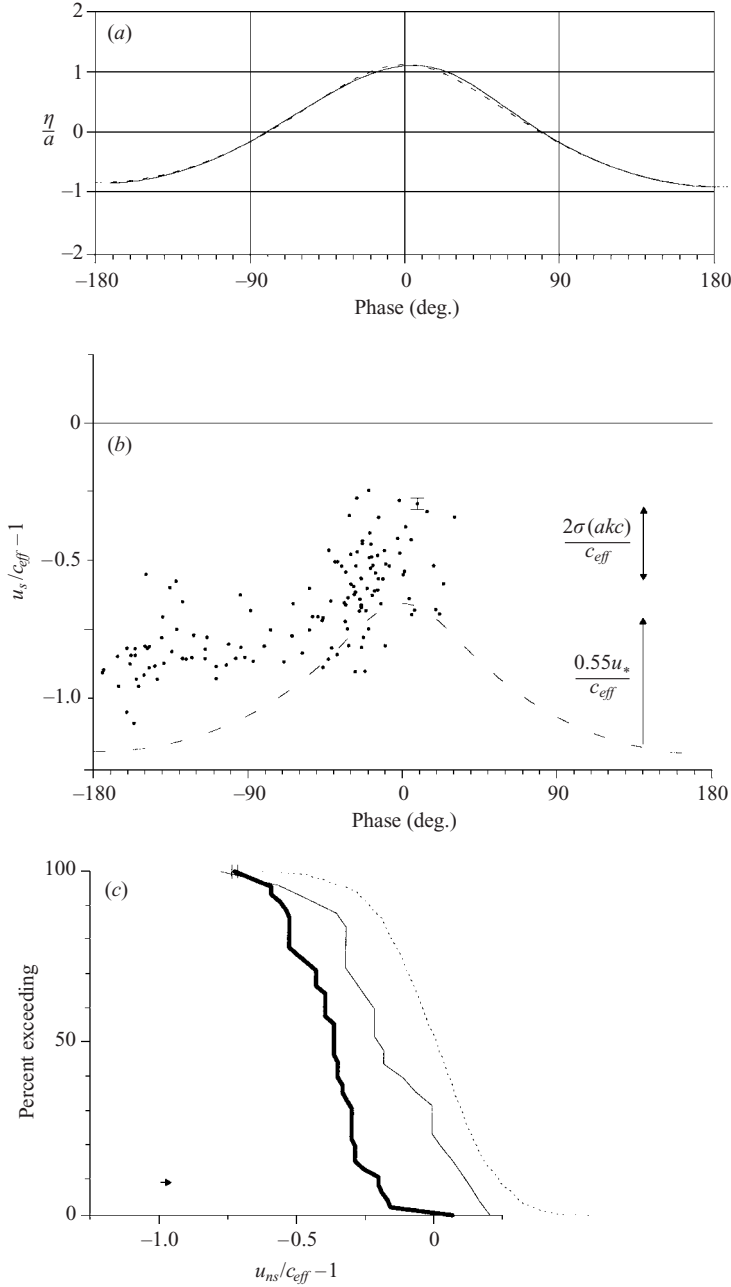
FIGURE 7. As figure 3 but at a fetch of 4.35 m and a wind speed of $8.1\,\mathrm{m\,s^{-1}}$.

the surface of waves with wavelengths of between 70 and 200 mm. Consequently, PIV measurements were undertaken at two levels of resolution. The approximate sizes of the flow fields imaged by the camera system at these two scales are shown superimposed on figure 1. At the higher resolution, particle positions and velocities could be accurately determined within $100\,\mu\mathrm{m}$ of the interface, while at the lower resolution, the influence of larger-scale processes on the viscous sublayer could

be observed. The two sets of PIV measurements were undertaken using different techniques and yielded complementary information, as described in the following sections.

4.1. *PIV Measurements at* 12 μm *pixel resolution*

At the higher resolution, flow in the immediate vicinity of the surface was visualized within a region of approximately 16.2 by 13.0 mm. Special software was developed to enable direct displacement measurements to be made on the captured particle images at the camera resolution. Clear reflections of subsurface particles could be observed under the relatively smooth windward faces and crests of the waves. For small angles of view relative to the horizontal, the position of the interface could be located reliably at the midpoint between a particle and its reflection. Given the laser pulsing frequency, both the velocity and location of individual particles relative to the surface could be determined. The local surface velocity was obtained by extrapolating to the water surface using an assumed linear velocity distribution through pairs of adjacent data points. It is noted that reliable measurements were not possible within two regions along the waves. Within the highly turbulent spilling region, the velocities are very high and the flow behaviour is exceedingly complex, precluding the use of this system to accurately quantify the near-surface behaviour. Also, just upwind of the trough, the horizontal water particle velocities are very small and it was difficult to accurately discern particle depths below the interface, particularly when the surface was moving rapidly in a vertical direction.

Coincident images of the water surface profile were captured by a CCD camera of lower resolution, mounted rigidly above the PIV camera and viewing the water surface from above. The laser light sheet created a well-defined line in the water surface. This optical property defining the interface was used to provide measurements of the water surface profile and hence the phase location for the 12 μm resolution subsurface images.

Approximately 140 surface velocity and tangential stress measurements were obtained for each experiment (row 22). It was found that the measured surface velocities yielded a significantly different picture of the surface velocity distribution than that reported by O82. We observed the distribution of the surface velocity structure along the windward faces of the waves and our measured surface velocity values at the crest were substantially lower than the mean total wave speed. These low values contrast with the theoretical model of incipient breaking of Banner & Phillips (1974), but this appears to be due to differences between surface layer flows associated with breaking onset and post-breaking configurations.

To achieve an acceptable degree of accuracy in the measured tangential stresses, BP98 found it essential to conduct the subsurface imaging at very small scale. The coincident wave profiles available from the camera images captured above the surface revealed that a significant proportion of the measurements (approximately 40% to 70%) of the near-crest velocity and tangential stress data had been gathered on waves with a maximum steepness exceeding 0.5 and therefore were presumably breaking (Banner 1990).

The development of the surface skin flow along the windward face of the waves is shown in figure 8. Velocity measurements obtained within $\pm 15°$ of the $-90°$, $-45°$ and $0°$ phase points have been binned in 50 μm bins from the free surface. A large number of data points are in close proximity to the surface (50% are at less than 150 μm depth). There is no indication of very strong shear immediately adjacent to the surface as the velocity measurements at depths less than 50 μm do
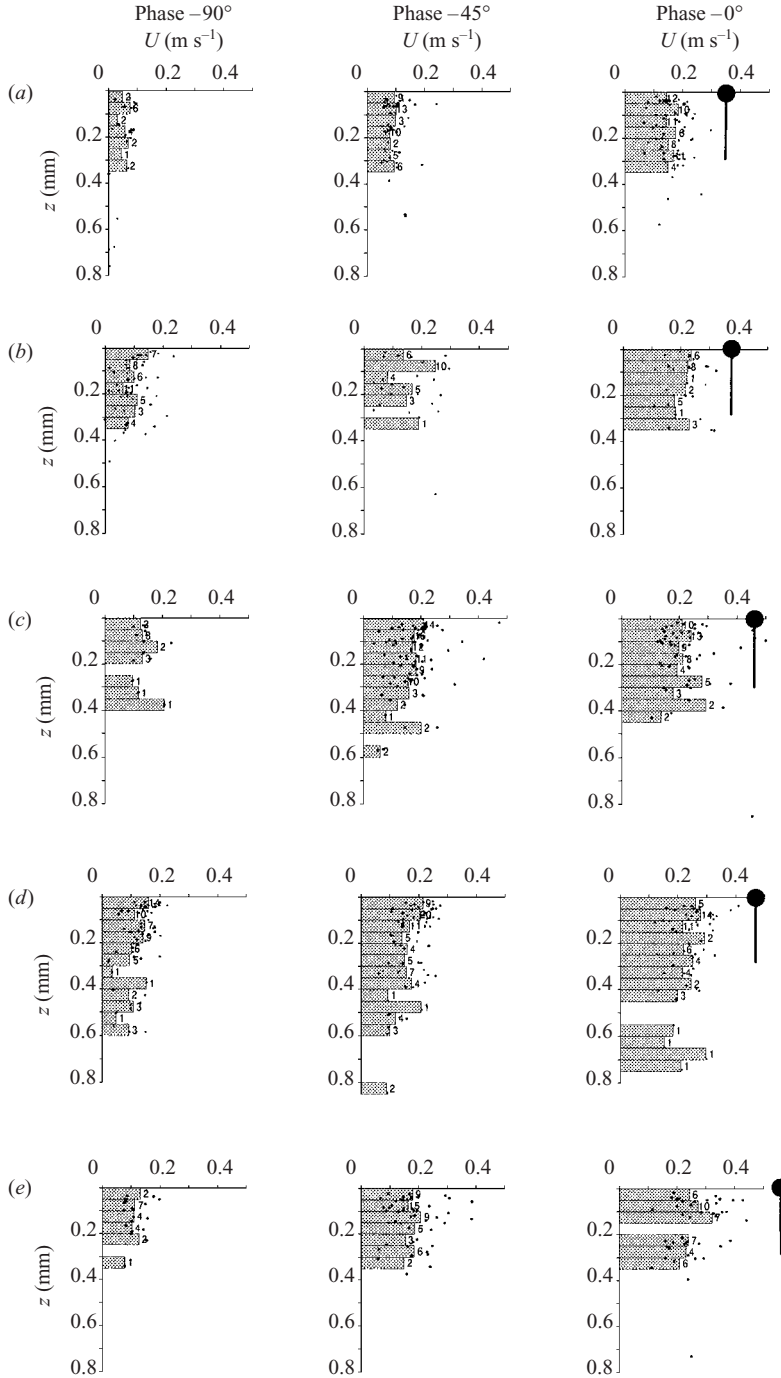
FIGURE 8. Development of the surface skin flow along the windward face of microscale breaking waves at fetches and wind speeds of: (*a*) 4.35 m, 4.8 m s^{-1}; (*b*) 2.45 m, 6.3 m s^{-1}; (*c*) 4.35 m, 6.3 m s^{-1}; (*d*) 2.45 m, 8.1 m s^{-1}; (*e*) 4.35 m, 8.1 m s^{-1}. In each panel, the total wave speed is shown at zero wave phase by a line with a solid circle head. Note that the sizes of hydrogen bubbles and beads used by Okuda (1982) were 0.14 mm and 0.7 mm respectively.

not exhibit substantially higher velocities. At a given wind speed, the results shown in figure 8 indicate only small changes in the mean crest surface velocity with fetch. With increasing fetch, there is a systematic downshift in wave frequency with a corresponding increase in wave speed. Consequently, mean crest surface skin flow speed is reduced relative to the wave speed as the waves lengthen with increasing fetch.

Further details of the surface velocities obtained by the high-resolution camera system are given in figures 3(b) to 7(b), which show the observed velocities along the wave phase. The number of measurements obtained for each case investigated is shown in row 22 of table 1. These velocities have been normalized by the mean wave speed c_{eff} and are shown relative to a frame of reference moving with the wave itself. Theoretical estimates obtained from a comparable fifth-order Stokes wave are also shown. Four interesting results can be derived from these figures:

(i) The average surface velocities over the windward faces of these microscale breaking waves are substantially greater that those derived from the Stokes theory. If the Stokes theory is accepted as representing the contribution of the wave orbital motion, this difference can then be attributed to the surface drift formed either directly by the wind-induced skin friction or by the wake flow associated with the spilling region. The mean measured drift on the crests and windward faces of these waves was observed to range from $(0.23 \pm 0.02)u_*^a$ in the troughs up to $(0.33 \pm 0.07)u_*^a$ at the crest.

(ii) Whereas O82 argued that the surface drift was abruptly modulated at the crests of breaking waves (figure 2), our measurements do not support that view. In two cases (figures 3 and 4), there appears to be a steady increase in both the mean phase-averaged surface drift, approaching a doubling in magnitude from trough to crest. In all other cases, the mean surface drift at the trough increases by less than 50% towards the crest over the windward faces of the waves.

(iii) The Stokes fifth-order velocity estimates appear to provide a natural lower bound to the velocity data.

(iv) Our surface velocity measurements show that there is substantial variability in the instantaneous surface velocity around the mean drift up to approximately $\pm 0.17 u_*^a$ in the trough and $\pm 0.37 u_*^a$ at the crest. The observed fluctuations in the surface velocity may be due to group modulation of the wave field, fluctuations in the skin friction or turbulence in the wake of the spilling region. The data set allows the relative contributions of these processes to be assessed. The wave records were processed to yield estimates of the linear crest and trough orbital velocity akc. The r.m.s variability in akc is shown in row 21 of table 1 and is superimposed in figures 3(b) to 7(b). In the troughs, the variability in akc is comparable with the observed variability in the surface velocity measurements, suggesting that this variability is due primarily to the modulation of the wave field associated with wave groups. At the crests, the variability in the surface velocities increases relative to the magnitude of the variability in akc, suggesting an increase in the relative contribution of fluctuations in the skin friction or near-surface turbulence generated by the wind drift layer or in the wake of the spilling region.

4.2. *PIV measurements at* $35\,\mu$m *pixel resolution*

The field of view of the $12\,\mu$m pixel resolution system was too confined to observe the local surface velocity in relation to the larger-scale, subsurface flow field. Our investigation of the larger-scale flow structures required increasing the field of view captured by the subsurface camera. Its lens was replaced by a Micro Nikkor lens

with a focal length of 60 mm, yielding a subsurface field of view of approximately 45×37 mm, as illustrated in figure 1. This arrangement yielded negligible optical distortion. Also, because the subsurface camera now provided sufficient waveform contextual information, the above-surface camera was not needed. The increased field of view implied a corresponding reduction in the precision of the velocity and position measurements. The resolution of the subsurface images was reduced to approximately 35 μm. Particle reflections were still used to indicate the proximity to the interface of these velocity measurements but without the precision previously available. Unlike with the previous 12 μm pixel resolution measurements, co-located tangential stress measurements were not possible.

Many hundreds of images were captured and reviewed with the specific objective of resolving the fundamental issue of the direction of the motion of the surface drift at the crest relative to the waveform. Consequently, the surface velocity behaviour of a specific subset of the wave populations was examined, namely, those waves exhibiting local slope values greater than 0.5 on their downwind face. The local slope was determined from the subsurface images on length scales of millimetres rather than the resolution of fractions of a millimetre used to determine the wave statistics shown in table 1. Therefore it is expected that these samples were obtained from the very steepest subset of the entire wave population. An image was only processed, and a crest velocity measurement obtained, if the downwind face of the wave was sufficiently steep and near-surface (< 350 μm depth) particles were present at the wave crest. If near-surface particles were also visible downwind of the crest, a second velocity measurement was also undertaken. The number of images processed in this way is shown in row 23 of table 1.

The images obtained using this measurement system provided a much broader perspective on the overall flow structure beneath microscale waves. Representative images and their computed flow fields are presented and discussed subsequently in this paper.

Figure 9 below illustrates the processing steps in our image analysis methodology. Figure 9(*a*) is the original flow visualization showing the rich flow structure beneath the crest and forward face of a microscale breaking wind wave at a fetch of 4.35 m forced by a wind speed of 8.1 m s^{-1}. Figure 9(*b*) shows superimposed local measurements of velocity within 350 μm of the surface at the crest and downwind of the crest indicated at points A and B. This figure also shows PIV measurements of velocity throughout the subsurface domain. The PIV measurements were obtained using multi-pulse, single-frame autocorrelation analyses of the flow visualizations, as described in detail in Peirson (1998).

Also clearly visible in figure 9(*b*) is a zone of intense fluid shear localized at the toe of the spilling region. The flow within the spilling region contains the highest velocities and is the site of the most intense turbulence – four clear, consecutive individual particle track images cannot be observed in this region. The light sheet half-width was approximately 0.5 mm and the time between the first and last pulses was approximately 6 ms. This implies that the velocity component normal to the plane of view can be estimated to be at least 15% of the streamwise value within the spilling region. In this image, intense regions of illumination generated by the locally highly curved surface can also be observed.

The lowest panels of figures 3(*c*) to 7(*c*) show distributions of ensembles of measurements of near-surface velocities measured at the crests of steep waves using a wider angle of view of the subsurface region. Row 23 of table 1 shows the number of images captured and analysed. Presented together with these are distributions of

W. L. Peirson and M. L. Banner

(*a*)

(*b*)

Highly turbulent flow

A B

Intense shear
at toe

50 100 150
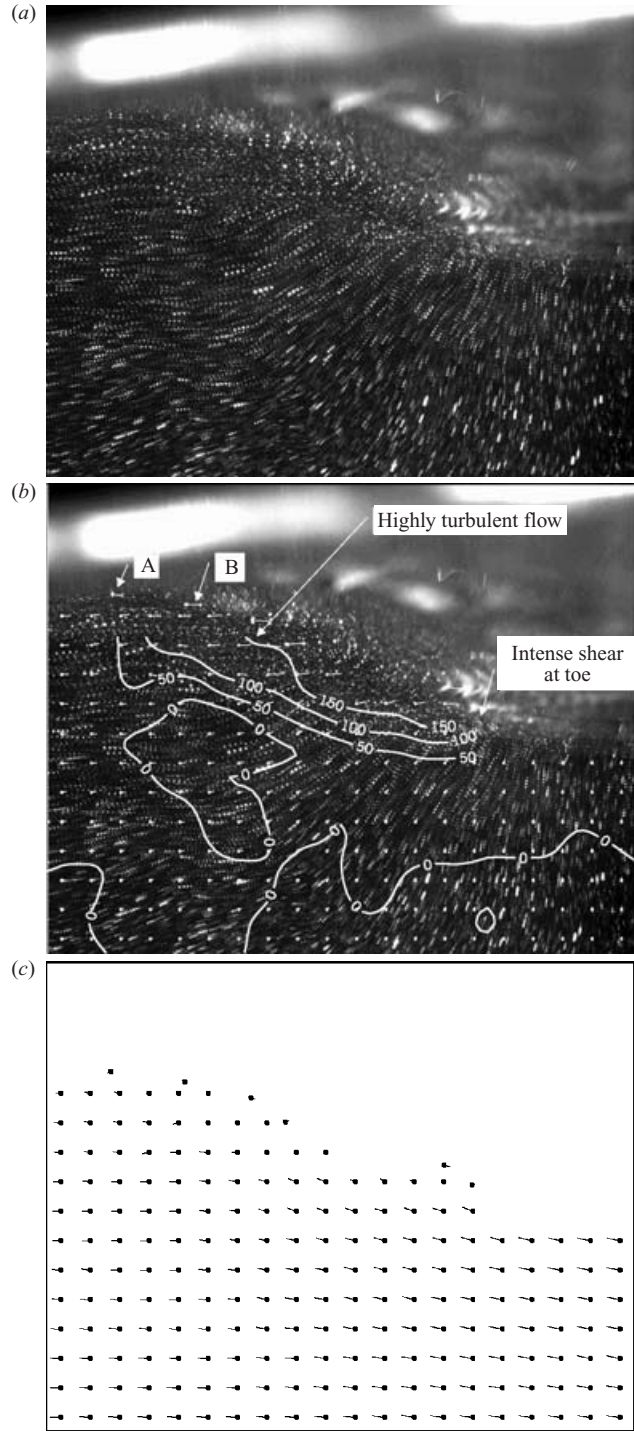50 150
0 100 100
0 50 50
0

0 0
0

(*c*)

FIGURE 9. For caption see facing page.

near-surface velocity measurements downwind of the crest and wave speeds obtained from the zero-crossing analysis. Wave speed distributions for waves with forward slopes greater than 0.5 were also extracted and the mean speed was found to differ by less than a few percent from the mean speed of the entire wave population.

A major finding arising from our study of the surface layer kinematics was that, in a frame of reference travelling with the wave, surface transport at the crest of breaking microscale wind waves was predominantly in an upwind direction. This finding is contrary to the extrapolations presented in O82.

4.2.1. *Crest surface fluid velocities compared with wave speeds*

Our ensemble of results on crest fluid speed is shown in the lowest panels of figures 3(*c*) to 7(*c*). It is immediately apparent that the distributions of near-surface velocity at the crest and the measured wave speeds exhibit a similarity of form. However, the mean values of near-surface velocity at the crest are only between 70% and 80% of the mean wave speeds, indicating a significant difference between crest fluid and wave speeds. Based on these measured distributions, for transport to take place downwind over the crest relative to the moving waveform, the highest crest velocities must be associated with the slowest waves. Even if such a restrictive assumption is invoked, only approximately 25% of waves at the higher wind speeds would satisfy this condition. Hence, we concluded that the characteristic spilling region behaviour of microscale breaking wind waves is for the spilling region to remain compact and restricted to very limited portion of the overall wave surface and downwind of the crest.

There are two potential sources of errors in our measurements of crest surface fluid velocity. (*a*) Reflections in the wave surface indicated that the mean depth of our near-surface measurements was $110\,\mu$m. Based on the tangential stress measurements presented in BP98, the mean correction needed to extrapolate these near-surface velocities to obtain a surface value is less than $0.02\,\mathrm{m\,s^{-1}}$. These corrections, indicated by the small arrows in the lower panels of figures 3(*c*) to 7(*c*), are seen to be negligible. It is also evident from our measurements that there is a strong, local acceleration of surface layer flow ahead of the crest towards the spilling region. This is evident in the substantially increased velocities measured downwind of the crest relative to those at the crest as shown in the lower panels of figures 3(*c*) to 7(*c*). (*b*) The errors associated with the limited resolution of the particle displacement measurements are shown in each of the lower panels of figures 3(*c*) to 7(*c*). These also are negligible relative to the differences in observed crest fluid velocity and the measured wave speed.

Overall, as noted earlier, the speed and complexity of the flow in the spilling region made it difficult to visualize the flow in spite of the high temporal and spatial resolution of our instrumentation. Independent estimates obtained by Peirson (1998) indicate

FIGURE 9. (*a*) Original PIV visualization of the flow inside a microscale breaking wind wave crest obtained at a fetch of 4.35 m and a wind speed of $8.1\,\mathrm{m\,s^{-1}}$. Approximate image size is 43.0 mm by 34.3 mm. Wind and wave directions are both towards the right. (*b*) The flow visualization in (*a*) with PIV velocity vectors and vorticity contours $(\mathrm{s^{-1}})$ superimposed. Vector spacing on regular grid is 2.15 mm. The particle motions used for measurement of near-surface velocities at the crest and downwind of the crest are labelled A and B respectively. Note the intense fluid shear at the toe of the spilling region and the highly turbulent nature of the spilling region wake. (*c*) Subsurface velocity field as in (*b*) but in a frame of reference travelling with the wave. The vectors were derived by subtracting C_{eff} from the horizontal components of the velocity vectors shown in (*b*). Note the substantial spilling region with local fluid speeds equal to the wave speed, yet the transport is rearward at the crest relative to the moving wave.

that, from momentum flux considerations, the spilling region is well-approximated dynamically as a very thin, compact layer riding on the forward face of the microscale breaking wave and exposed to intense shear stresses.

4.3. *Subsurface flow visualizations*

From the many hundreds of flow visualization images examined, representative images were selected to highlight more general characteristics of the flow field beneath these small waves. In figures 9(*b*), 10(*b*), and 11(*b*), these visualizations were analysed using PIV techniques to characterize the local velocity field structure. Subsurface flow fields beneath waves are often better understood in a frame of reference moving with the waves. Consequently, the PIV velocity vectors are also shown in figures 9(*c*), 10(*c*) and 11(*c*) with the total wave speed c_{eff} subtracted from the horizontal component of velocity. In some subsurface images (examples are shown in figures 9, 10 and 11), surface rupture was clearly evident at the toe of the spilling region.

In figure 9, rupture of the surface is occurring with the spilling region moving rapidly over the water surface ahead of the toe (as noted in figure 9*b*). In a fixed reference frame, the flow ahead of the toe indicates negligible horizontal transport. In a frame moving with the wave (figure 9*c*), water can be observed being carried along within the spilling region. The velocity vectors show a direct and rapid subduction of water ahead of the toe by the spilling region. Note also the rearward transport of water at the crest in this frame of reference and the highly turbulent wake due to the shear layer beneath the spilling region.

Similar general behaviour can also be observed in figure 10. The spilling region is again substantial in size, with rapid subduction occurring beneath its toe as it propagates over the water surface. In this case, the flow beneath the crest is much more turbulent (figure 10*c*). It is interesting to note the strong difference in the strength of the turbulence in the wake of the spilling region that extends in a layer approximately 6 mm deep, in contrast to the much weaker turbulence in the fluid below. High levels of shear can also be observed beneath the wake. It should also be noted that rearward transport occurs relative to the wave at the crest.

Surface rupture can also be observed in figure 11. In this case, the size of the spilling region is much smaller, its wake is far less turbulent and, relative to the wave profile, the flow is again rearward at the wave crest. It is of interest to note that rotational particle motions can be observed downwind of the toe of the spilling region at location D in figure 11(*b*) that may be indicative of parasitic capillary activity.

In some images, strong vorticity was also observed downwind of the crest, consistent with the presence of parasitic capillary waves (figure 12). While the location of the surface can easily be found at the crest using the clear particle reflections in the surface, its location is more difficult to detect precisely further downwind due to the highly curved sarface. The motion of a highly curved portion of the surface has been

FIGURE 10. (*a*) Original flow visualization of flow inside a microscale breaking wind wave crest obtained at a fetch of 4.35 m and a wind speed of 8.1 m s^{-1}. Approximate image size is 45.5 mm by 36.4 mm. Wind and wave directions are towards the right. (*b*) Flow visualization of (*a*) with PIV velocity vectors and vorticity contours (in s^{-1}) imposed. Vector spacing on regular grid is 2.28 mm. Note the surface rupture and intense shear at point C and the extensive, highly turbulent region in its wake below the wave crest (D). (*c*) Subsurface velocity field of (*b*) in a frame of reference travelling with the wave. Velocity vectors were derived by subtracting c_{eff} from the horizontal components of the velocity vectors shown in panel b. Note the extensive spilling region. Note also that flow at the crest is rearward relative to the moving wave.
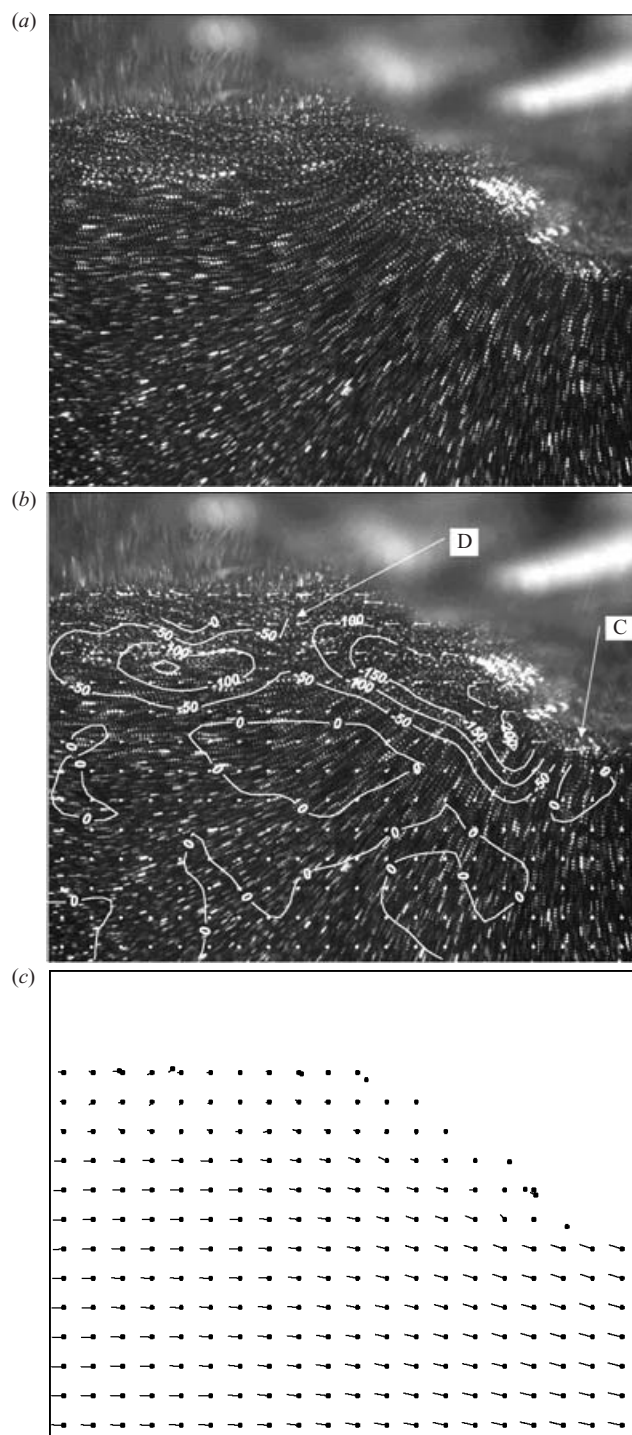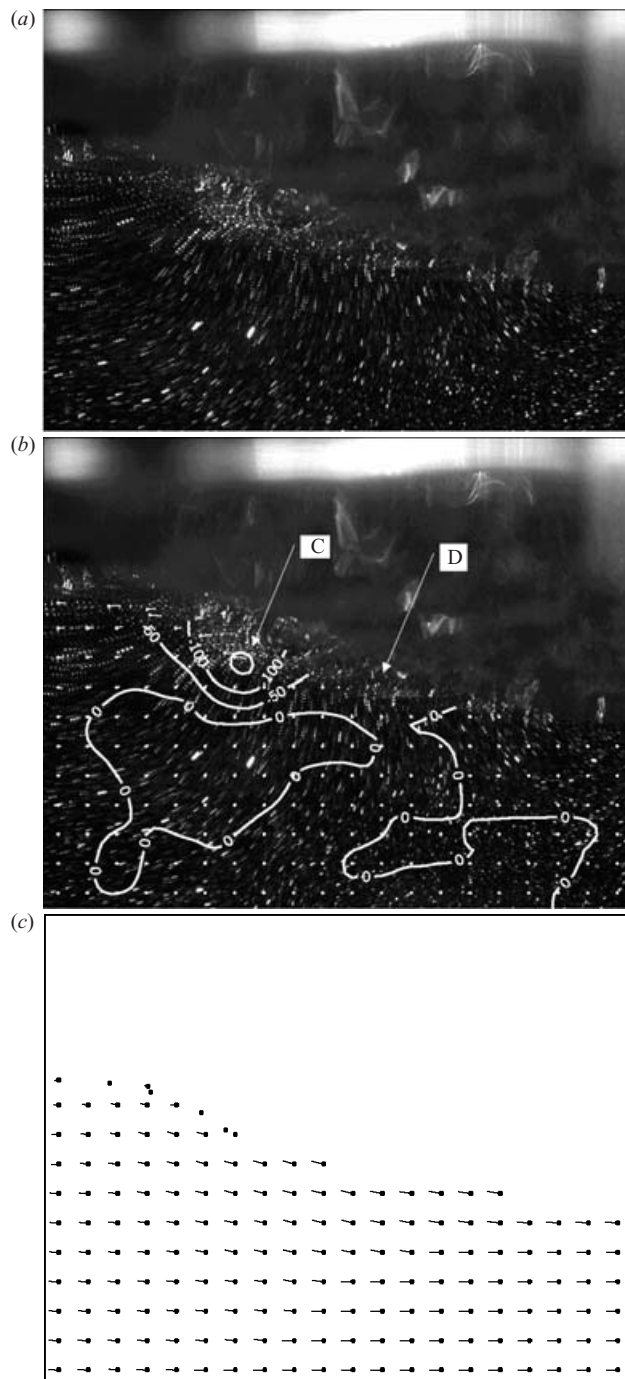
FIGURE 10. For caption see facing page.

FIGURE 11. As figure 10 but at a wind speed of $6.3\,\mathrm{m\,s^{-1}}$. In (*b*) note the surface rupture at point C and the highly turbulent region in its wake. The highly curved particle paths at point D may be indicative of parasitic capillary activity. In (*c*) note the substantial spilling region, yet at the far left of the image, the flow at the surface is rearward relative to the moving wave.
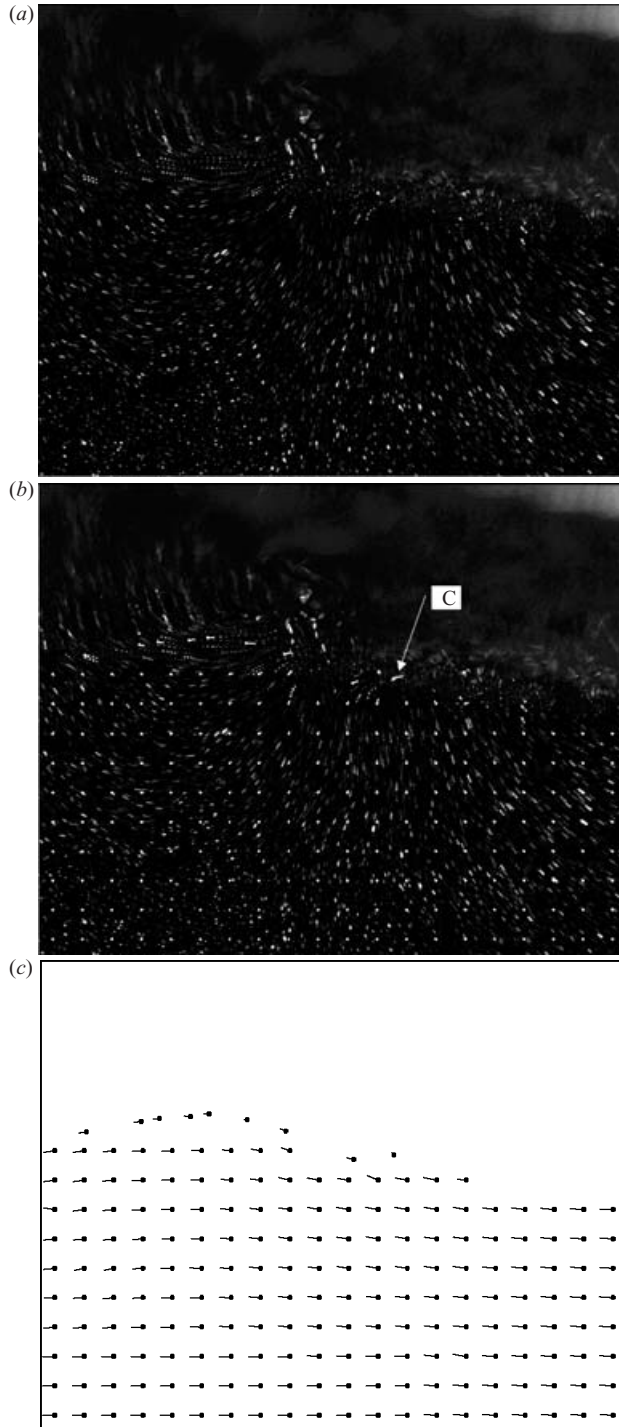
FIGURE 12. (*a*) As figure 10 but at a wind speed of $4.8\,\mathrm{m\,s^{-1}}$. Approximate image size is 43.0 mm by 34.3 mm. In (*b*) vector spacing on regular grid is 2.15 mm. C indicates a curved surface feature travelling at the wave speed consistent with parasitic capillary activity. Note in (*c*) that at two points on the surface of the wave, the fluid has achieved a velocity very close to the wave speed.

captured at location C. In a frame travelling with the wave, it can be seen in figure 12(c) that the velocity at two points on the surface downwind of the crest is very close to the mean total wave speed.

The strong surface convergence observed at the toe of the spilling region of microscale breaking waves (figures 9 to 11) may be contrasted with the much weaker observed surface divergence on the upwind face. Here, we quantify surface convergence as $-\partial u/\partial \xi$, a measure of the rate at which surface fluid is subducted, where ξ is a coordinate parallel to the surface. In §4.1 we observed that there is a change in mean surface drift along the windward faces of the microscale breaking waves from $(0.23 \pm 0.02)u_*^a$ in the trough increasing to $(0.33 \pm 0.07)u_*^a$ at the crest. This change in surface drift takes place over a distance of $\lambda/2$ and yields mean values of surface divergence along the windward face of between 0.2 and $1.3\,\mathrm{s}^{-1}$.

At the toe of the spilling region, the surface convergence is very large ($> 175\,\mathrm{s}^{-1}$). Figure 13 shows two images in which surface divergence is apparent, presumably due to local variations in the wind-generated tangential stress. Figure 13(a) is typical of the observed surface skin flow. Local divergence at the surface is fairly weak. However, as shown in figure 13(b), rapid spatial changes in surface skin flow were occasionally observed. For this image, the surface divergence was estimated as approximately $8\,\mathrm{s}^{-1}$. For such breaking conditions, the rate of divergence induced by variations in surface tangential stress is far weaker than the convergence produced at the toe of spilling regions.

5. Discussion

5.1. *Key processes*

The measurements reported here allowed us to identify in our laboratory microscale breakers the dominant transport processes associated with surface aqueous viscous sublayers and their ability to disrupt the aqueous sublayers. These key properties, annotated in figure 14, are described in detail below.

5.1.1. *Surface transport*

Previous measurements based on floating markers provide a kinematic description of the surface skin of wind-forced waves that may be influenced by spurious effects. To avoid the problems associated with floating markers, we used PIV techniques to measure phase-related mean wind drift in the wave troughs of $(0.23 \pm 0.02)u_*^a$, increasing along the windward faces to $(0.33 \pm 0.07)u_*^a$ at the crest. The surface drift directly wind induced is substantially less than the surface drift of $(0.50 \pm 0.02)u_*^a$ found in the absence of wind waves by BP98. The wind-induced surface drift is also substantially less than measured values of the total drift $(0.50 \pm 0.05)u_*^a$ determined in the presence of wind waves using floating drifters (Keulegan 1951; Phillips & Banner 1974; Wu 1975; amongst others). Contributions to the transport of surface-bound materials are also made by windage, Lagrangian drift associated with these nonlinear waves and capture and advection by the spilling regions, but the relative importance of these other transport processes remains unclear. The physical size of the spilling regions and the nature of the surface convergence at the toe are such that surface transport and entrainment of floating materials will be strongly dependent on their size, surface-active properties and buoyancy. These properties profoundly affect their transport at the point of subduction beneath the spilling regions of microscale breaking wind waves.
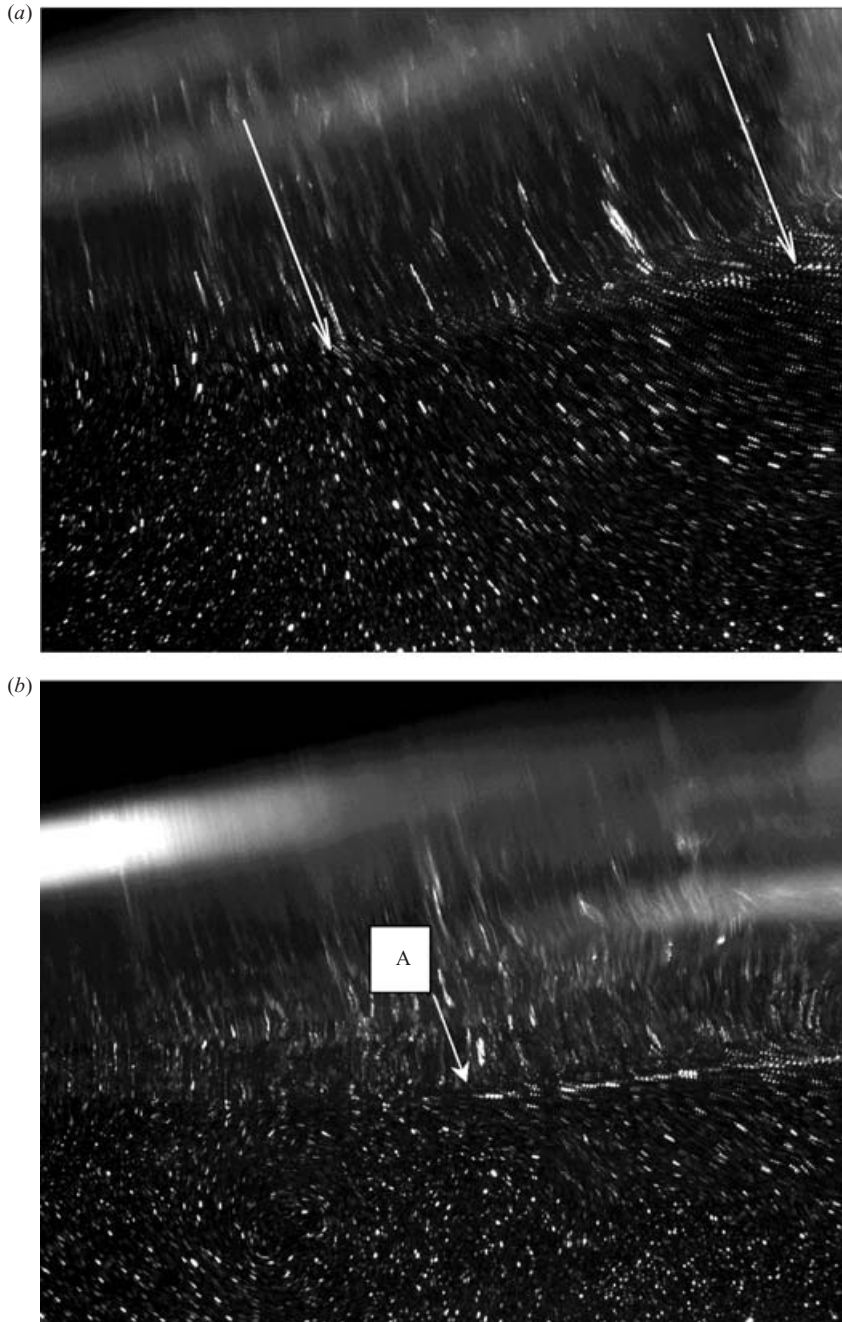
(a)

(b)

FIGURE 13. Two flow visualizations beneath the windward face of a wind wave obtained at a fetch of 4.35 m and a wind speed of $6.3\,\mathrm{m\,s^{-1}}$. In both visualizations the location of the surface is indicated by the arrow heads. Surface divergence can be observed in both images. In (b) the surface divergence at A is estimated to be approximately $8\,\mathrm{s^{-1}}$. Approximate image sizes are 45.5 mm by 36.4 mm.

The measurements show that the spilling region rarely extends to the crest of the wave. This simplifies considerably our view of the structure of transport along the surface of microscale breaking wind waves.
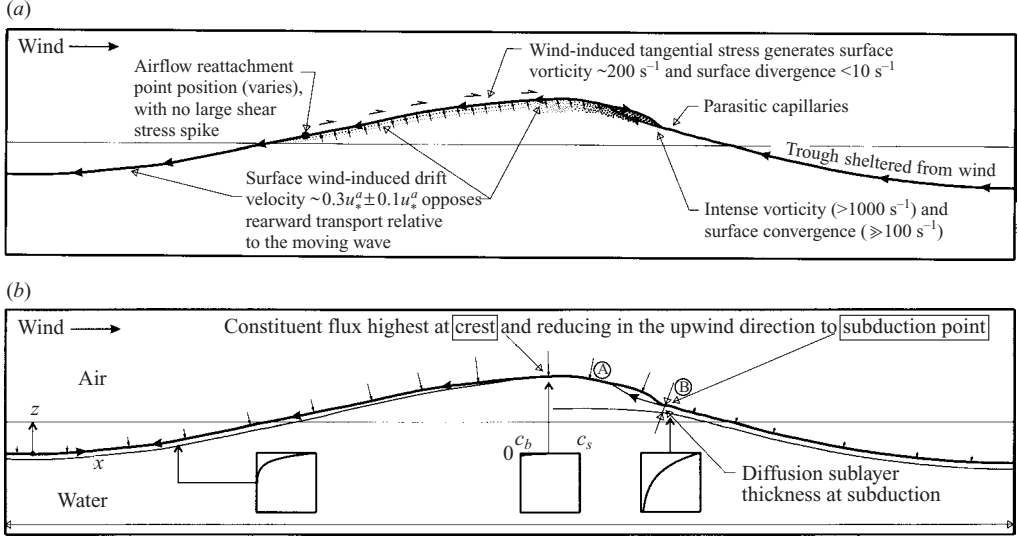
(*a*)

(*b*)

FIGURE 14. (*a*) The surface flow kinematics beneath microscale breaking wind waves as revealed by this investigation and annotated accordingly. Note the relatively small contribution of the tangential stress forcing and the compact nature of the spilling region. This schematic can be contrasted with that shown in figure 1. (*b*) Schematic of constituent transfer from air to water in the presence of microscale breaking. Beneath the spilling region, the very thin diffusion sublayer is subducted and mixed to a relatively large depth so that the residual concentration near the surface is very small. Except at the spilling region, surface fluid travels rearward relative to the wave and the diffusion sublayer thickens with increasing residence time at the surface. The arrows indicate the estimated distribution of constituent flux from air to water.

5.1.2. *Subduction of fluid beneath the spilling region*

The intense, localized surface convergence at the leading edge of spilling regions of microscale breakers, with the associated subduction of fluid beneath the spilling region was observed to be the dominant surface disruption process. A large ensemble (~ 200) of visualizations of the surface flow was examined and it was found that both the strength and frequency of disruption due to breaking was much higher than that due to intensified local divergence events on the windward faces of microscale breakers.

The observations and measurements obtained during this investigation show that the dominant process in the generation of intense, localized surface convergence is subduction of fluid beneath the spilling region. If spilling occurs downwind of the crest, it produces an intense and localized convergence of surface water at the toe. This subduction directly injects constituents previously concentrated in the surface layers into a region of intense turbulent mixing. This is seen clearly in figures 9 and 10 by the highly turbulent flow within the crest region in contrast to the fluid below. These measurements show that the surface convergences associated with microscale breaking regularly exceed values of $100 \, \text{s}^{-1}$.

5.1.3. *Surface divergence features of the surface layer flow*

O82 and Csanady (1990, hereafter referred to as C90) argued that strong divergence of surface fluid takes place at the point of reattachment of the airflow on the upwind face. In the present study, we confirmed that divergence can be observed on the upwind

faces of the waves. For wind speeds up to $8\,\mathrm{m\,s^{-1}}$, the mean divergence was observed to be between 0.2 and $1.3\,\mathrm{s^{-1}}$, with peak values not exceeding approximately $10\,\mathrm{s^{-1}}$.

5.1.4. *Near-surface vorticity induced by parasitic capillary structures*

High levels of near-surface vorticity were observed during this study on the downwind faces of microscale waves, apparently due to the presence of parasitic capillary structures. These near-surface vorticity features occur in the immediate vicinity of the surface and may be sufficient to disrupt the aqueous diffusion sublayer. Detailed measurements and characterization of these structures will require much higher spatial and temporal resolution measurement techniques. Nevertheless, our observations confirm that the magnitudes of the surface convergence and vorticity generated by parasitic capillary waves are much less than those generated by microscale breaking. As a consequence, microscale breaking is expected to make a much greater contribution to disruption of the surface diffusive sublayer than parasitic capillary activity.

5.1.5. *Near-surface turbulence*

We observed that intense levels of vorticity ($> 1000\,\mathrm{s^{-1}}$) are generated at the toes of the spilling regions of microscale breaking wind waves, with concomitant intense shear layers with high turbulent intensity levels. Also, from the results of BP98, we know that surface layer shear levels reaching $600\,\mathrm{s^{-1}}$ can be generated by the wind-induced tangential stress in the aqueous linear sublayer. However, values of vorticity greater than $200\,\mathrm{s^{-1}}$ were not observed outside the aqueous linear sublayer except in the immediate vicinity of the toes of spilling regions. The spilling regions themselves are thin ($< 2\,\mathrm{mm}$ thickness) and are bounded by shear layers in the airflow above and in the water below. The mixing within the spilling regions is exceedingly vigorous and the rapid exchange between surface and interior fluid within these regions makes them local regions of particularly high rates of interfacial constituent exchange.

5.2. *Implications for air–water exchange*

Our observations have enabled us to assess the relative importance of processes that disrupt the surface viscous sublayer at moderate wind speeds and correct a number of key misconceptions regarding the kinematics of microscale breaking wind waves. We now explore the significance of the surface processes induced by microscale breaking waves for air–water gas exchange.

From the results of O82, C90 developed a viscous roller model of the air–sea gas transfer by microscale breaking wind waves which yielded an analytic expression for constituent exchange as a function of Schmidt number and the effective surface area in gas transfer. The model is based on an active surface roller structure that extends over approximately 35% of the surface area of the wave, centred on the wave crest. The model roller is forced by intense viscous stresses along the roller surface. According to this model formulation, surface divergence and convergence zones of equal intensity distributions persist upwind and downwind of the roller. The model predicted that the surface divergence zone results in a thinning of the diffusion sublayer, thereby enhancing local surface constituent flux and creating a dominant surface region that determines the overall constituent transfer rate.

The C90 model, in conjunction with the development of the infrared imaging systems, has directed the attention of interfacial exchange investigations to the upwind faces of microscale breaking wind waves. However, there are disparities between the conclusions of C90 and recent laboratory observations, particularly S2001. On

the basis of their laboratory observations, S2001 proposed that vorticity generated within the spilling regions and swept rearward is responsible for disrupting the thin thermal sublayer on the upwind faces and creating a cool skin layer locally.

Our observations provide a contrasting viewpoint that addresses these issues and have motivated a new perspective on constituent interfacial exchange driven by microscale breaking wind waves. For example, C90 assumed an extensive surface roller covering 35% of the surface, yet our observations show that the surface spilling region rarely extends upwind of the crest whilst the toe of the spilling region generally occupies a phase point of approximately $+45°$ relative to the crest. The spilling region therefore occupies less than 15% of the surface of actively breaking waves. Also, C90 assumed approximately equal intensities of convergence and divergence on either side of the roller whereas our observations show that the magnitude of the convergence beneath the spilling region is many times greater than the magnitude of the divergence on the upwind face. Also, the overall area of the surface does not change greatly due to the presence of waves (Jähne & Haußecker 1998, p. 453). Therefore, the removal rate of water elements from the surface at highly localized and intense subduction points must be balanced by dilation of surface elements within spatially extensive regions of much weaker surface divergence, as shown by our measurements.

In contrast with the observations made by S2001 at much larger scale, our observations indicate that subsurface turbulence is relatively ineffective at maintaining a thin thermal sublayer on the upwind faces. Instead, a weak mean surface divergence superimposed with localized and more intense wind-induced divergences are the primary processes responsible for the thin thermal sublayer.

Our observations have allowed us to develop an alternative method to estimate the mean transfer velocity k_v of a low-solubility airborne constituent into the underlying water column via the aqueous surface diffusive sublayer mediated by microscale breaking wind waves.

5.2.1. *Order-of-magnitude analysis*

We begin by considering the aqueous concentration field $C(x,z,t)$, assumed quasi-two-dimensional, immediately beneath the free surface in a vertical two-dimensional slice with the x-axis following the surface and aligned with the wave direction and travelling with the waves (figure 14*b*), with z the upward local surface-normal coordinate. The effects of surface curvature in this surface-following system are assumed to be negligible. C_s is the concentration, assumed constant, at the surface in the water phase and C_b is the concentration in the bulk of the water below. The advection–diffusion equation takes the form

$$\frac{\partial C}{\partial t} + u\frac{\partial C}{\partial x} + w\frac{\partial C}{\partial z} - D\frac{\partial^2 C}{\partial x^2} - D\frac{\partial^2 C}{\partial z^2} = 0, \tag{1}$$

where D is the (constant) molecular diffusivity.

Initially, to determine the upper bound for this mechanism, we assume that the diffusive sublayer is disrupted on the forward face of every wave by continuous breaking and the flow kinematics are approximately steady, $\partial C/\partial t = 0$. We explore the implications of breaking intermittency subsequently. Using the two-dimensional continuity equation and the identities

$$u\frac{\partial C}{\partial x} = \frac{\partial(uC)}{\partial x} - C\frac{\partial u}{\partial x}, \tag{2}$$

$$w\frac{\partial C}{\partial z} = \frac{\partial(wC)}{\partial z} - C\frac{\partial w}{\partial z}, \tag{3}$$
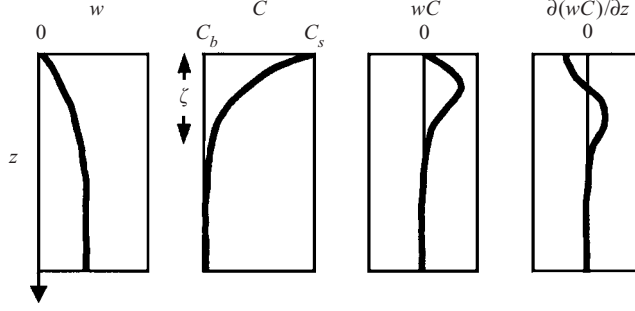
FIGURE 15. Schematic distributions of w, C, wC and $\partial(wC)/\partial z$ adjacent to a surface subject to surface divergence. The thickness of the diffusion sublayer (ζ) is indicated. Note that the mean value of $\partial(wC)/\partial z$ of zero across the diffusion sublayer arises from the boundary values of w and C and their indicated distribution within the sublayer.

(1) reduces to

$$\frac{\partial(uC)}{\partial x} + \frac{\partial(wC)}{\partial z} - D\frac{\partial^2 C}{\partial x^2} - D\frac{\partial^2 C}{\partial z^2} = 0. \tag{4}$$

We can now undertake an order-of-magnitude analysis of each term in (4). The appropriate length scales, where $O()$ denotes order, are $\delta x = \lambda = O(0.2\,\text{m})$, $\delta z = O(0.2\,\text{mm})$ for the diffusion sublayer thickness (e.g. Münsterer, Mayer & Jähne 1995). Hence changes in concentration δC are $O(C_s - C_b)$, where the molecular diffusivities D are $O(10^{-8}\,\text{m}^2\,\text{s}^{-1})$.

Two estimates for quantifying changes in the term uC in the x-direction are available. In both cases, we assume that the mean near-surface concentration across the diffusion sublayer is approximately zero immediately behind the spilling region (figure 14b, point A) and increases in an upwind direction to $O(C_s - C_b)$ immediately prior to subduction (figure 14b, point B). Changes in u can be estimated by two methods:

(i) the rearward surface velocity in a frame of reference moving with the wave is approximately zero immediately windward of the spilling region and increases in magnitude to $O(c_{\text{eff}})$ at the toe of the next breaking wave in the upwind direction;

(ii) alternatively, from the data we can estimate the change in velocity to be approximately $0.1u_*^a$ along half the wavelength between trough and crest along the windward face.

These estimates provide similar magnitudes for uC of $O[0.5^*c_{\text{eff}}(C_s - C_b)]$.

The term $\partial(wC)/\partial z$ requires careful consideration. Except at the toe of the spilling region, w is strictly zero at the surface and increases in magnitude away from the surface, as shown in figure 15. In contrast, outside the diffusion sublayer the difference between the local concentration and that in the bulk is zero and increases to $(C_s - C_b)$ as the surface is approached. We wish to assess the magnitude of $\partial(wC)/\partial z$. Figure 15 shows schematic distributions of w and C in the presence of a surface divergent flow. For small z, recalling that the diffusion sublayer is much thinner than the viscous sublayer, we have

$$w \approx \frac{\partial w}{\partial z}z = -\frac{\partial u}{\partial x}z, \tag{5}$$

using the continuity equation.

From our surface velocity measurements along the windward faces of the waves, we know that the mean surface divergence $\langle \partial u / \partial x \rangle$ is of order $0.5\,\mathrm{s}^{-1}$ while peak values were observed of order $10\,\mathrm{s}^{-1}$. However, as shown in figure 15, the gradients in w and C adjacent to the surface are opposite in sign and the overall change in the quantity wC is zero across the diffusion sublayer. We are interested in the integrated local contribution across the diffusion sublayer and while the quantity $\partial(wC)/\partial z$ is $O(0.5(C_s - C_b))$ immediately below the surface (figure 15), its integrated value across the diffusion sublayer is $O(0)$, i.e. negligible, along the entire windward face.

Suppressing the common factor $(C_s - C_b)$ in each term, the relative importance of each term is as follows:

$$\frac{\partial(uC)}{\partial x} \sim 1\,\mathrm{s}^{-1}, \quad \frac{\partial(wC)}{\partial z} \sim 0\,\mathrm{s}^{-1}, \quad D\frac{\partial^2 C}{\partial x^2} \sim 2.5 \times 10^{-7}\,\mathrm{s}^{-1}, \quad D\frac{\partial^2 C}{\partial z^2} \sim 0.25\,\mathrm{s}^{-1}.$$

This suggests that two dominant terms determine the exchange rate at the air–sea interface and their physical role may be understood as follows:

(i) $\partial(uC)/\partial x$: rearward flux of concentration along the diffusion sublayer towards the subduction point at the intense surface convergence at the toe of the spilling region.

(ii) $D\partial^2 C/\partial z^2$: constituent diffusion from the surface into the aqueous sublayer.

On the basis of these results, we constructed a model for estimating interfacial exchange rates, as described in the following subsection.

5.2.2. *Estimates of interfacial exchange*

Figure 14(b) shows a schematic description of the underlying physics of this model. For simplicity we make the following assumptions: (i) surface water travels rearward relative to the moving waveform and is relatively undisturbed except immediately upwind of and within the spilling region, with the influence of surface divergence on the windward face assumed to be negligible; (ii) beneath the spilling region, the diffusion sublayer, encapsulated within the viscous sublayer, is mixed over a relatively large depth called the *subduction zone*.

The surface layer velocity measurements show that in a frame of reference moving with a microscale breaking wave, the surface fluid approaches the spilling region at a speed of approximately $c - bu_*^a$, where c is the wave speed and b is a value bounded between 0.2 and 0.4 signifying the strength of the surface drift. We solve the following equation based on the dominant terms within the diffusion layer as discussed above:

$$\frac{\partial(uC)}{\partial x} - D\frac{\partial^2 C}{\partial z^2} = 0, \tag{6}$$

with $u = -(c - bu_*^a)$. This equation has the solution

$$C = (C_s - C_b)\,\mathrm{erfc}\left(|z|\sqrt{\frac{bu_*^a - c}{4Dx}}\right) + C_b, \tag{7}$$

where erfc is the complementary error function and $x = 0$ just upwind of a spilling region and becomes more negative as we move along the wave surface upwind to the next spilling region. We note that the complementary error function can be approximated by a linear function ranging from $C = C_s$ at $z = 0$ to $C = 0.1(C_s - C_b) + C_b$ at $z = -0.9\sqrt{4Dx/(c - bu_*^a)}$, with an accuracy of $\pm 0.1(C_s - C_b)$.

At the point of subduction, the representative thickness of the diffusion sub-layer will have developed to a value of $\zeta = 0.9\sqrt{4D\lambda/(c - bu_*^a)}$. According to this approximation, $\sim 80\%$ of the total constituent transferred by direct surface flux will remain trapped within the depth ζ of the surface until it is dispersed beneath the spilling region.

From conservation of mass, the downward vertical constituent flux through the surface of the wave (from a crest upwind to the toe of the next spilling region) equals the streamwise transverse flux within the diffusion sublayer at the point of subduction beneath the toe of the spilling region. This is illustrated in figure 14(*b*). Therefore,

$$(C_s - C_b)k_v\lambda = \left(\frac{C_s + 0.1(C_s - C_b) + C_b}{2} - C_b\right)\frac{\zeta(c - bu_*^a)}{0.8} \tag{8}$$

or

$$k_v\lambda = 0.69\zeta(c - bu_*^a). \tag{9}$$

For the range of conditions examined during our experiments, the quantity $\lambda/(c - bu_*^a)$ ranged from approximately $1.2/f$ to $1.5/f$, where f is the mean intrinsic frequency of the microscale breaking waves. Substituting and rearranging, we obtain

$$k_v = (1.0 \to 1.15)\sqrt{Df}. \tag{10}$$

This estimated value of k_v must be regarded as an upper bound for the transfer velocity, having been derived for continuously breaking waves of characteristic intrinsic frequency f. In naturally occurring situations, several factors will reduce this estimated value of k_v, including: (i) spatial and temporal intermittently of the microscale breaking process; (ii) the short-crested nature of microscale breaking waves; (iii) residual constituent concentrations in the surface layer.

The significance of breaking intermittency and short-crestedness can be assessed with reference to our laboratory wave measurements of the breaking probability at a given fetch (table 1, row 20, expressed as the passage rate of breaking crests as a proportion of the passage rate of all crests with both observed within the same frequency band around the peak). It is worth noting that the breaking rate used here can be directly related to the fraction of total surface area subducted per unit time at the microscale breaking fronts (see Phillips 1985, equation (6.2)). This measurement reflects the breaking intermittency as well as the short-crested nature of the waves. If the waves are breaking randomly and intermittently with probability p and $|x|$ is the mean length of unbroken surface, the quantity $|x|/(c - bu_*^a)$ increases to between $1.2/(pf)$ and $1.5/(pf)$, and k_v is modified as follows:

$$k_v = (1.0 \to 1.15)\sqrt{pDf}. \tag{11}$$

Also, in our laboratory experiments, microscale breaking waves were observed to occur in wave groups in which the number of waves in a group was generally between 5 and 10 (figure 16). If microscale wave breaking remains localized near the peaks of the wave groups, this localization of the subduction process will further reduce the transfer velocity. This is associated with the existence of much thicker diffusion sublayers in the non-breaking regions. Indicative calculations showed that there is a potential reduction in transfer velocity of about 20% due to wave group effects.

For CO_2 at $20°$, $D \approx 8 \times 10^{-8}\,\mathrm{m^2\,s^{-1}}$ and over the range of our experimental conditions, estimated values of ζ range between 0.29 and 0.38 mm. Based on the
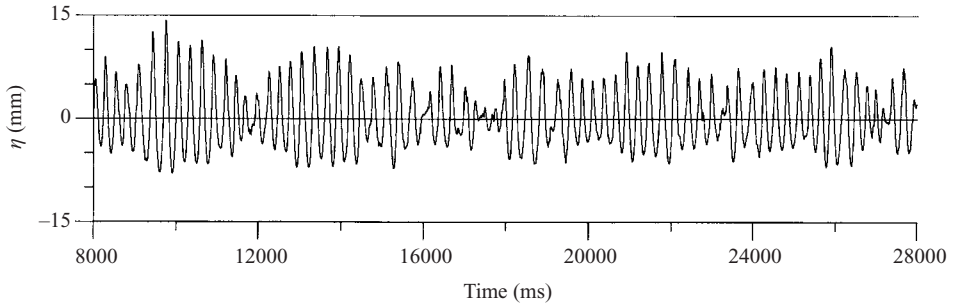
FIGURE 16. Time series record of surface elevation in mm obtained from a capacitance wave probe showing the recorded group structure of microscale breaking wind waves generated by a wind of 8.1 m s^{-1} at a fetch of 4.35 m.

earlier discussion in this section, the associated transfer velocities are estimated to range from 90 cm h^{-1} up to 200 cm h^{-1}. The lower transfer velocities are predicted for strong wind drift cases ($b \sim 0.4$) and sporadic wave breaking due to modulating wave groups. The higher transfer velocities are envisaged for weak wind drift ($b \sim 0.2$) and a quasi-uniform distribution of breaking over the surface.

These transfer velocity values are 1.5 to 3 times larger than values observed in laboratory tank experiments (see Komori, Nagaoa & Murakami 1993 for a compilation of observed values). This indicates that microscale breaking is potentially a very effective process in the enhancement of constituent transfer, as has been observed to occur for wind speeds 10 m above the surface $U_{10} \geqslant 5$ m s^{-1}, and exceeds by a wide margin the transfer velocities associated with any previously proposed mechanisms. These differences between our estimated values and observed values can be reconciled by considering the spatial distribution of microscale breaking processes in laboratory tanks and the effects of residual concentrations in the surface layers.

5.2.3. *The spatial distribution of microscale breaking in laboratory tanks*

Microscale breaking structure and probabilities depend significantly on the fetch in laboratory tanks at moderate wind speeds. At very short fetches ($\lesssim 2$ m), only capillary ripples are present and there are no microscale breaking waves. In the absence of microscale breaking, a zone of low interfacial transfer could be expected to occur with rates similar to those obtained from the Deacon (1981) model. Once microscale breaking waves develop (at 2–3 m fetch), with increasing fetch there is a downshift in their intrinsic frequency and a decrease in breaking probability, hence the passage rate of breaking waves is a changing function of fetch at a given wind speed. Table 1 shows a relative reduction of order 15% in the breaking probability from 2.45 to 4.35 m fetch at wind speeds of 8.1 and 6.3 m s^{-1}, with almost all waves microscale breaking at 2.45 m fetch. Equation (6) above predicts that the transfer velocity will also decrease with fetch from the point of microscale wave development. This prediction is consistent with the measurements and observations of Wanninkhof & Bliven (1991) who investigated constituent transfer dependence on fetch. It should also be noted that Caulliez (2002) recently also reported a decrease in breaking rate of the dominant waves between 15 m and 26 m fetch at a wind speed of 13 m s^{-1}. In this case, the waves were not of microscale size but were longer air-entraining, breaking short gravity waves. Our kinematic measurements were made at fetches between 2 m and 5 m where the highest rates of constituent transfer would be expected to occur.

The validation of the proposed levels and fetch dependence that follows from our model predictions awaits future experimental validation.

5.2.4. *Residual concentrations in the surface layers*

To this point we have assumed that the diffusion sublayer is mixed over a relatively large depth during the subduction process. However, microscale breaking is a cyclic process with the intensity of the breaking varying during the breaking cycle (Banner 1988). Our observations in this paper have shown that intense breaking will mix fluid to depths of several millimetres beneath the surface (see for example, figure 9). If breaking is weak, residual concentrations may remain very close to the surface layer and reduce the apparent transfer velocity derived from concentration measurements taken centimetres beneath the surface. The significance of residual concentrations remaining adjacent to the surface in the surface transfer rates over a range of fetch and wind conditions remains to be determined.

The results of our study are consistent with the surface temperature distributions observed by S2001, although the visualization results they presented were obtained for considerably stronger wind forcing ($11 \, \mathrm{m \, s^{-1}}$) than in our experiments. Where the waves were not breaking, crest surface skin temperatures were lower than those in the presence of microscale breaking waves e.g. figure 8 in S2001. The thermal pattern in that figure reflects a well-developed diffusive sublayer that has not been subducted by breaking on the forward faces of the waves. The highest surface temperatures are observed to occur on the upwind faces and crests of the waves where surface divergences occur and local surface velocity fluctuations due to the varying surface tangential stress or near-surface turbulence in the wake of the spilling region. Note also that the subsurface vorticity levels measured by S2001 are approximately an order of magnitude less than those measured at the surface by BP98 and in the present investigation.

In the presence of microscale breaking, a thermal signature can be observed in the data of S2001 that is consistent with our suggested behaviour of the diffusive sublayer. The highest surface temperatures are seen in their images to occur on the wave crests, extending from upwind of the crest to immediately upwind of the toe of the spilling region with the lowest temperatures occurring immediately downwind of the spilling region (e.g. S2001, figure 9). This is consistent with subduction of a relatively thick diffusive sublayer beneath the spilling region accompanied by surface divergence induced by the breaking, bringing relatively warm interior fluid to the surface on the crests and upwind faces of microscale breaking wind waves. Smaller, localized surface divergence cells can also be observed, presumably due to fluctuations in the surface tangential stress or turbulence in the wake of the spilling region similar to structures observed during our investigations.

The strong correlation between interfacial exchange and fractional area coverage of microscale wave breaking (discussed in the introduction) is also entirely in accord with the findings of this investigation. As suggested by C90, the regions that yield highest rates of surface flux are those where the diffusion sublayer is thinnest and such regions provide the thermal signatures observed in the infrared imagery.

In summary, we have proposed a microscale breaking model for the exchange of constituents between air and water under moderate wind forcing. This model predicts that microscale breaking is potentially extremely efficient at enhancing air–sea exchange, with rates exceeding other proposed processes. The validity of the idealized model presented here, as well as an assessment of the significance of residual surface

layer concentrations on the transfer process, need to be validated through suitably designed laboratory experiments.

6. Conclusions

We have used PIV techniques to measure the phase distribution of the mean wind drift velocity along microscale breaking wind waves under laboratory conditions. The mean surface drift is found to increase from $(0.23 \pm 0.02)u_*^a$ in troughs along the windward faces to values of $(0.33 \pm 0.07)u_*^a$ at the crest. This is substantially less than the mean drift of $(0.50 \pm 0.02)u_*^a$ in the absence of wind waves reported by BP98. This value is also substantially less than measured values of the total drift $(0.55 \pm 0.05)u_*^a$ determined in the presence of wind waves using floating drifters (Keulegan 1951; Phillips & Banner 1974; Wu 1975; amongst others). Although we have quantified the wind-induced drift, the relative contributions to the transport of surface-bound materials associated with the other contributions to the total drift (windage, Lagrangian drift associated with these nonlinear waves and capture and advection by the spilling regions) remains unclear.

About the mean level of the surface drift, there is substantial variability in the instantaneous surface velocity up to approximately $\pm 0.17u_*^a$ in the trough and $\pm 0.37u_*^a$ at the crest. This variability can be attributed primarily to the modulation of the wave field, with additional contributions arising from fluctuations in wind forcing and near-surface turbulence generated by shear in the drift layer or by microscale breaking. Estimates of the surface current modulation due to the group structure of the wave field were able to account for almost all of the observed variability in surface current in the trough.

We have examined the suggestion in O82 that the viscous sublayer flow on the windward face of microscale breaking waves flows over the crest and feeds into the spilling region. The results of this study show that this is not the typical behaviour. Rather, the spilling region downwind of the crest generally remains locally compact, with a strong convergence of surface fluid at the toe and relatively weak divergence near the crest and on the upwind face of that wave. Surface layer fluid is transported upward from the interior flow into the spilling region at a location immediately upwind of the spilling region and downwind of the crest.

Previous investigators of air–water exchange processes have observed that constituent exchange across the interface is enhanced in the presence of wind waves. This study has shown that the physical behaviour and surface processes of microscale breaking wind waves are fundamentally different to those of smooth interfaces and clearly identifies those processes that result in failure of smooth solid wall parameterizations. Several previous studies have endeavoured to relate interfacial exchange rates to surface renewal characteristics of subsurface turbulence. Transfer rates of low-solubility gases, however, are controlled by the behaviour of the surface diffusive sublayer and such surface renewal approaches do not directly include surface rupture by breaking and associated intense surface convergence and vorticity.

Based on an order-of-magnitude analysis, a simple model is proposed to estimate the additional constituent flux associated with the presence of microscale breaking wind waves. The model results indicate that microscale breaking is potentially a very effective process in the enhancement of constituent transfer observed to occur for $U_{10} \geqslant 3.8 \, \text{m s}^{-1}$ in open waters and exceeds by a considerable margin the transfer rates associated with previously proposed mechanisms. Also, the predicted fetch

dependence of the interfacial exchange due to microscale breaking is in qualitative agreement with laboratory observations.

Appendix. Wave measurements

Measuring the properties of microscale breaking waves is greatly complicated by their advection by the wind drift current. During this investigation, we developed a novel wave probe technique to directly measure the characteristics of the microscale breaking wind waves. Averages of the measured wave characteristics are presented in table 1 of the main paper and row references below refer to this table.

Two precisely parallel high-resolution capacitance wire probes were aligned vertically and deployed in the wind wave tank with their common axis in the downwind direction. Their outputs were digitized individually at a rate of 1 kHz. The temporal and spatial resolution capabilities of these probes resolved clearly the presence of parasitic capillaries downwind of the spilling regions. The spacing of the probes was measured *in situ* as 18.00 ± 0.07 mm using our high-resolution camera system (as described in §4 of the main paper).

During our experiments, characteristic wind waves were well-defined at each fetch and wind speed condition (except at a wind speed of $4.8 \, \text{m s}^{-1}$ and 2.45 m fetch for which only capillary ripples were present). It was possible to process the high-resolution wave probe records to obtain individual waveforms from each probe record delineated by crossings of the mean water level. Individual waves were defined as two successive negative-going crossings of the local mean water level. To extract the required local geometrical characteristics of the waves, negative-going zero crossing analysis was used as the upwind surfaces of wind waves are consistently smoother and more easily identified than other features (crest, trough) of the microscale breaking wave profiles. Phase ensemble averages of successive waves were constructed, with the negative-going zero crossing nominally identified with $-90°$ phase. Each individual probe record yielded the total wave energy density (row 7), a mean observed frequency (row 8) and wave height (row 9) from the two probes which were indistinguishable within the measurement error bounds.

By differencing the time of arrival of zero-crossing events on the upwind faces of waves propagating past the wire array, the total speed of individual waves (intrinsic wave speed plus wave transport due to wind drift) relative to a fixed frame of reference could be measured. The total speeds of individual waves were averaged to obtain a mean total speed c_{eff} (row 14). Note that in this measurement, no assumptions regarding the relationship between total wave speed, wavelength or wave frequency are made.

It was necessary to apply limits to the individual total wave speeds to ensure that a wave detected by one probe corresponded to the wave detected subsequently by the other probe. Sensitivity testing of these limits showed that the computed value of c_{eff} varied by less than 1% if the limits were changed from $\pm 30\%$ to $\pm 70\%$ of c_{eff}. Of the entire wave population, 25% and 15% of waves respectively were excluded by these limits, so we undertook further investigation of the properties of the waves that were being excluded. The mean frequencies and wave heights were recorded for the

accepted and rejected populations with the acceptance limits set at $\pm 70\%$. As shown in rows 11 and 12, the mean height of the rejected population was less than 60% and their mean frequency was at least 30% higher than of the corresponding statistics of the entire wave population. There is a group structure to the wave field and these rejected waves are associated primarily with surface ripples between the wave groups with dominant carrier wave heights.

The focus of this investigation is on the behaviour of the larger, more strongly breaking wind waves. As shown in rows 15 and 16, the mean height of those waves whose speeds could be determined was up to 11% higher than the entire population mean values and their frequency was 3% to 5% lower than the entire population mean. These differences are due to the elimination of the ripples from the wave population.

At each wave probe, we were also able to measure the time between the two zero-crossings defining an observed individual wave. Assuming that the waves change their length relatively slowly in comparison with their intrinsic frequency, the wavelength of an individual wave is the time between negative zero-crossings multiplied by the total wave speed. Again, no assumptions regarding relationships between total wave speed, wavelength or wave frequency are made.

Wavelengths obtained by this method were averaged and are presented in row 17. The local mean wavelength was also measured from ensembles of photographs of representative wave profiles. These two independent wavelength estimates were in agreement to within $\pm 20\%$. The mean and root-mean-square (rms) wave steepness are given in rows 18 and 19.

The total speed of the waves (c_{eff}) has two components: the intrinsic phase speed and an advective component associated with the wind drift current. Available theoretical methods for relating wave characteristics to phase speed rely on assumptions of steady, symmetrical wave trains and irrotational flow whereas the waves examined here are strongly modulated and asymmetrical, with their irrotational state disturbed by active microscale breaking and surface layer shear.

Using the local wavelength and steepness, equivalent linear and finite wave slope phase speeds (Longuet-Higgins 1978) can be calculated. However, resolution of the relative contributions of wave propagation speed and drift current are not necessary for this investigation. The issue of primary importance in our study is the motion of the surface skin relative to the overall waveform: relative to a stationary observer, this is the local speed of the waveforms, c_{eff}. Also, following BP98, the percentage of breaking waves was determined based on the maximum slope on the leeward wave face exceeding 0.5. The estimated numbers of breaking waves are shown in row 20.

Previously, it has been very difficult to achieve direct, rapid and precise measurements of wave speed and wavelength, particularly for wave systems with group structure. Our approach provides a simple, direct and accurate means of measuring microscale breaking wave characteristics.

REFERENCES

BANNER, M. L. 1988 On the mechanics of spilling zones of quasi-steady breaking water waves. In *Sea Surface Sound* (ed. B. R. Kerman), pp. 63–70. Kluwer.

BANNER, M. L. 1990 The influence of wave breaking on the surface pressure distribution in wind–wave interactions. *J. Fluid Mech.* **211**, 463–495.

BANNER, M. L., JONES, I. S. F. & TRINDER, J. C. 1989 Wavenumber spectra of short gravity waves. *J. Fluid Mech.* **189**, 321–344.

BANNER, M. L. & PEIRSON, W. L. 1998 Tangential stress beneath wind-driven air–water interfaces. *J. Fluid. Mech.* **364**, 115–145 (referred to herein as BP98).

BANNER, M. L. & PHILLIPS, O. M. 1974 On the incipient breaking of small scale waves. *J. Fluid Mech.* **65**, 647–656.

CAULLIEZ, G. 2002 Statistics of geometric properties of breaking wind waves observed in laboratory. *Gas Transfer at Water Surfaces.* AGU Geophysical Monograph 127, pp. 31–37.

CSANADY, G. T. 1990 The role of breaking wavelets in air–sea gas transfer. *J. Geophys. Res.* **95**, 749–759 (referred to herein as C90).

DEACON, E. L. 1981 Sea–air gas transfer: the wind speed dependence. *Boundary Layer Met.* **21**, 31–37.

DUNCAN, J. H. 1981 An experimental investigation of breaking waves produced by a towed hydrofoil. *Proc. R. Soc. Lond.* A **377**, 331–348.

DUNCAN, J. H. 2001 Spilling breakers. *Annu. Rev. Fluid Mech.* **33**, 519–547.

DUNCAN, J. H., PHILOMIN, V., QIAO, H. & KIMMEL, J. 1994 The formation of a spilling breaker. *Phys. Fluids* **6**, 2558–2560.

FEDEROV, A. V. & MELVILLE, W. K. 1998 Nonlinear gravity–capillary waves with forcing and dissipation. *J. Fluid Mech.* **354**, 1–42.

FEDEROV, A. V., MELVILLE, W. K. & ROZENBERG, A. 1998 An experimental and numerical study of parasitic capillary waves. *Phys. Fluids* **10**, 1315–1323.

JÄHNE, B. & HAUßECKER, H. 1998 Air–water gas exchange. *Annu. Rev. Fluid Mech.* **30**, 444–468.

JESSUP, A. T., ZAPPA, C. J. & YEH, H. 1997 Defining and quantifying microscale wave breaking with infrared imagery. *J. Geophys. Res.* **102**, 23145–23153.

KATSAROS, K. B. & ATATÜRK, S. S. 1992 Dependence of wave-breaking statistics on wind stress and wave development. In *Breaking Waves* (ed. M. L. Banner & R. H. J. Grimshaw) Springer.

KEULEGAN, G. H. 1951 Wind tides in small closed channels. *J. Res. Natl Bur. Stand.* **46**, 5, Research Paper 2207.

KOMORI, S., NAGAOA, R. & MURAKAMI, Y. 1993 Turbulence structure and mass transfer across a sheared air–water interface in wind-driven turbulence. *J. Fluid Mech.* **249**, 161–183.

LIN, J. & ROCKWELL, D. 1995 Evolution of a quasi-steady breaking wave. *J. Fluid Mech.* **302**, 29–44.

LONGUET-HIGGINS, M. S. 1978 Some new relations between Stokes' coefficients in the theory of gravity waves. *J. Inst. Maths Applics.* **22**, 261–273.

LONGUET-HIGGINS, M. S. 1992 Capillary rollers and bores. *J. Fluid Mech.* **240**, 659–679.

LONGUET-HIGGINS, M. S. 1995 Parasitic capillary waves: a direct calculation. *J. Fluid Mech.* **301**, 79–107.

LONGUET-HIGGINS, M. S. & TURNER, J. S. 1974 An 'entraining plume' model of a spilling breaker. *J. Fluid Mech.* **63**, 1–20.

MELVILLE, W. K. 1994 Energy dissipation by breaking waves. *J. Phys. Oceanogr.* **24**, 2041–2049.

MÜNSTERER, T., MAYER, H. J. & JÄHNE, B. 1995 Dual-tracer measurements of concentration profiles in the aqueous mass boundary layer. In *Air–Water Gas Transfer* (ed. B. Jähne & E. Monahan), pp. 637–648. AEON Verlag.

OKUDA, K. 1982 Internal flow structure of short wind waves, Part I. The vorticity structure. *J. Oceanogr. Soc. Japan* **38**, 28–42 (referred to herein as O82).

OKUDA, K., KAWAI, S. & TOBA, Y. 1977 Measurement of skin friction distribution along the surface of wind waves. *J. Oceanogr. Soc. Japan* **33**, 190–198 (referred to herein as O77).

PEIRSON, W. L. 1997 Measurement of surface velocities and shears at a wavy air–water interface using particle image velocimetry. *Exps. Fluids* **23**, 427–437.

PEIRSON, W. L. 1998 On the dynamics and kinematics of microscale-breaking wind waves. PhD. thesis, University of New South Wales.

PEIRSON, W. L. & BANNER, M. L. 2000 On the strength of breaking of deep water waves. *Coastal Engineering 2000* (ed. B. L. Edge), pp. 369–381. ASCE.

PEREGRINE, D. H. & SVENDSEN, I. A. 1978 Spilling breakers, bores and hydraulic jumps. *16th Proc. Conf. Coastal Eng., ASCE*, pp. 540–550.

PHILLIPS, O. M. 1985 Spectral and statistical properties of the equilibrium range in wind-generated gravity waves. *J. Fluid Mech.* **156**, 505–531.

PHILLIPS, O. M. & BANNER, M. L. 1974 Wave breaking in the presence of wind drift and swell. *J. Fluid Mech.* **66**, 625–640.

SIDDIQUI, M. H. K., LOEWEN, M. R., RICHARDSON, C., ASHER, W. E. & JESSUP, A. T. 2001 Simultaneous particle image velocimetry and infrared imagery of microscale breaking waves. *Phys. Fluids* **13**, 1891–1903 (referred to herein as S2001).

WANNINKHOF, R. H. & BLIVEN, L. F. 1991 Relationship between gas exchange, wind speed, and radar backscattar in a large wind wave tank. *J. Geophys. Res.* **96**, 2785–2796.

WU, J. 1975 Wind-induced drift currents. *J. Fluid Mech.* **68**, 49–70.

ZAPPA, C. J., JESSUP, A. T. & ASHER, W. E. 2001 Microscale wave breaking and air–water gas transfer. *J. Geophys. Res.* **106**, 9385–9391.